LIFT-OFF PERFORMANCE

IN FLEXURE PIVOT PAD AND

HYBRID BEARINGS

A Thesis

by

DAVID HUNTER MERTZ

Submitted to the Office of Graduate Studies of
Texas A&M University
in partial fulfillment of the requirements for the degree of

MASTER OF SCIENCE

December 2008

Major Subject: Mechanical Engineering

LIFT-OFF PERFORMANCE

IN FLEXURE PIVOT PAD AND

HYBRID BEARINGS

A Thesis

by

DAVID HUNTER MERTZ

Submitted to the Office of Graduate Studies of
Texas A&M University
in partial fulfillment of the requirements for the degree of

MASTER OF SCIENCE

Approved by:

Chair of Committee,	Dara Childs
Committee Members,	W. Lynn Beason
	Luis San Andrés
Head of Department,	Dennis O'Neal

December 2008

Major Subject: Mechanical Engineering

ABSTRACT

Lift-off Performance in Flexure Pivot Pad and
Hybrid Bearings. (December 2008)
David Hunter Mertz, B.S., Trinity University
Chair of Advisory Committee: Dr. Dara Childs

Three flexure pivot pad bearings (FPBs) with different preloads are evaluated for use in high performance applications by comparing them to a hybrid hydrostatic bearing (HHB). One application of these bearings is in turbopumps for liquid rocket engines. To evaluate bearing performance, the lift-off speed of the shaft from the bearing surface is experimentally determined. Experimental data of lift-off are collected using a circuit running through the shaft and the designed bearing. Other methods for measuring lift-off speeds were attempted but did not yield consistent results. Water is used as a lubricant to simulate a low viscosity medium.

In comparison to load-capacity-based predictions for FPBs, the experimental results showed lower lift-off speeds, higher load capacities, higher eccentricity ratios, and lower attitude angles. The bearings' predicted load capacity determined lift-off speed predictions, but the experimental results show no clear trend relating lift-off speed to load capacity. This was for a range of running speeds, with the *design speed* defined as the final speed in a particular test case.

At 0.689 bar supply pressure and for a design speed of 3000 rpm, the HHB showed greater load capacities and lower eccentricities than the FPBs, but the FPBs had lower lift-off speeds and attitude angles. In fact, the FPBs in the load-between-pad orientation outperformed the HHB in the load-on-pocket orientation with lower lift-off speeds for the shaft weight-only case. An increased supply pressure lowered the lift-off speeds in the HHB tests. If the load in the bearing application remains relatively small, a FPB could be substituted for an HHB.

DEDICATION

To my parents, Bruce and Mary Mertz, and to my grandparents and great-grandparents, who gave me the opportunity and encouraged me along the way. Also, to my Lord Jesus Christ for giving me the abilities and patience to complete this thesis.

ACKNOWLEDGEMENTS

Thanks to everyone who has helped me with my thesis and supported me along the way. First, to my family and friends for their encouragement. Thanks also to my professors, both in my undergraduate at Trinity University and during my graduate work at Texas A&M University. Thanks to my committee members, Dr. Childs, Dr. San Andrés, and Dr. Beason for all their patience and guidance in this process. Thanks to the guys at the Turbomachinery Laboratory—Henry Borchard, B.J. Dyck, David Klooster, and Eddie Denk. Finally, thanks to my girlfriend, Laura Beth Gonzales, for her encouragement and support.

TABLE OF CONTENTS

Page

Page

LIST OF FIGURES

Page

Page

Page

Page

LIST OF TABLES

Page

NOMENCLATURE

C_b	Bearing radial clearance [L]
C_p	Pad radial clearance [L]
C_{xx}, C_{xy}, C_{yx}, C_{yy}	Damping coefficients [F-T/L]
D	Diameter [L]
E	Modulus of elasticity [M/L^2]
e_x, e_y	Distance from bearing center [L]
f_{bx} , f_{by}	Force coefficients [F]
I	Area moment of inertia [L^4]
K_θ	Stiffness [F/L]
K_{xx}, K_{xy}, K_{yx}, K_{yy}	Stiffness coefficients [F/L]
L	Length [L]
m	Bearing preload, see Eq. 2 [dim]
M_{xx}, M_{xy}, M_{yx}, M_{yy}	Mass coefficients [M]
R_b, R_p, R_s	Bearing, pad, shaft radius (respectively) [L]
T	Temperature [Θ]
W	Load [F]
α	Bearing offset [dim]
β	Web angle measured from leading edge of pad
Δx , Δy	Perturbation displacement in x or y direction [L]
$\Delta\dot{x}$, $\Delta\dot{y}$	Perturbation velocity in x or y direction [L]
$\Delta\ddot{x}$, $\Delta\ddot{y}$	Perturbation acceleration in x or y direction [L]
ε	Bearing eccentricity [L]
ε_0	Bearing eccentricity ratio, see Eq. 7 [dim]
θ_p	Pad extent angle
μ	Dynamic viscosity [M/(L·T)]
ν	Kinematic viscosity [L^2/T]

1. INTRODUCTION

High-speed turbopumps require reliable bearings to support the shaft or rotor. One general type of bearing used in these applications is the hydrostatic bearing, which uses external pressurization to inject fluid into the bearing. A restricting orifice creates the pressure necessary to support the shaft in this type of bearing. The pocket pressure supports the shaft even when there is no rotation.

On the other hand, hydrodynamic bearings do not use orifice restriction. A thin fluid-film wedge develops as the shaft rotates, raising it off the bearing surface in a process called lift-off [1]. Since there is no need for external pressurization, hydrodynamic bearings eliminate a substantial cost to the end-user.

Bearing rotordynamic characteristics will be modeled using a combination of stiffness, damping, and mass coefficients. The following linearized force-displacement bearing model [2] is used for analysis:

$$-\begin{bmatrix} f_{bx} \\ f_{by} \end{bmatrix} = \begin{bmatrix} K_{xx} & K_{xy} \\ K_{yx} & K_{yy} \end{bmatrix} \begin{bmatrix} \Delta x \\ \Delta y \end{bmatrix} + \begin{bmatrix} C_{xx} & C_{xy} \\ C_{yx} & C_{yy} \end{bmatrix} \begin{bmatrix} \Delta \dot{x} \\ \Delta \dot{y} \end{bmatrix} + \begin{bmatrix} M_{xx} & M_{xy} \\ M_{yx} & M_{yy} \end{bmatrix} \begin{bmatrix} \Delta \ddot{x} \\ \Delta \ddot{y} \end{bmatrix} \qquad (1)$$

The use of this linear model is a common practice in the analysis of rotor-bearing systems [3]. Castigliano's theorem states that a neutrally stable elastic system must have a symmetric stiffness matrix [4]. The presence of skew-symmetric stiffness coefficients indicates the presence of destabilizing forces [4]. Subsynchronous vibrations are one result of destabilizing force in bearing systems. Tilting pad bearings (TPBs) significantly reduce or eliminate subsynchronous vibrations [5]. This type of bearing can be either hydrodynamic, hydrostatic, or hybrid (a combination of both). TPBs make use of pivots such that pads can rotate freely. A diagram of one type of TPB follows in Fig. 1.

This thesis follows the style and format of the ASME Journal of Tribology.

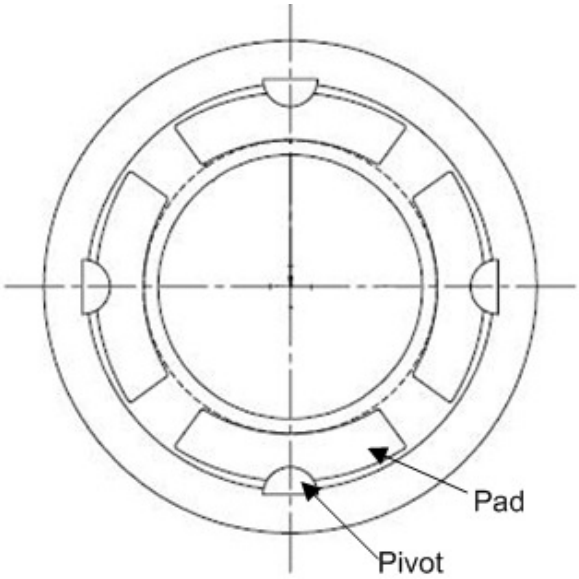

Fig. 1 Typical spherical seat TPB [6].

Even so, there are drawbacks to TPBs. These include wear at the pad pivot, tolerance stack up due to a more complex design, reduced damping, and difficulty of installation [7]. An alternative to TPBs are flexure pivot pad bearings (FPBs), also known as the flexible-pivot tilting-pad bearings. A FPB is machined as a single piece and uses a thin beam or web to support the bearing load. A typical FPB is shown in Fig. 2 and can be designed as either hydrodynamic, hydrostatic, or hybrid (combination of both). The rotational stiffness of the web allows for support while still flexing or tilting enough to reduce cross-coupled stiffnesses and reduce the likelihood of subsynchronous instabilities.

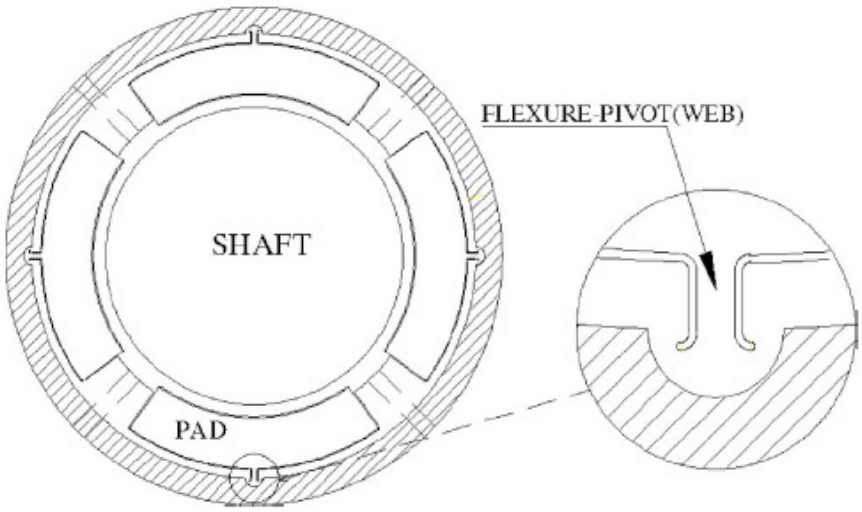

Fig. 2 Flexure pivot pad bearing [2].

Research Objective

The purpose of this project is to determine when a rotor lifts off in a hydrodynamic FPB and to compare its performance with a hydrostatic bearing. Bearing performance is determined through lift-off speed, load capacity, and the shaft position at design speed. The design speed is the running speed at the end of the speed ramp for a specific test case.

Need Statement

Some high-speed cryogenic turbopumps use hydrostatic bearings thus requiring external pressurization [8]. An experimental comparison between hydrodynamic FPBs and hydrostatic bearings should determine the circumstances under which current hydrostatic bearings can be replaced with hydrodynamic FPBs.

Overview

This thesis describes the design and testing of three FPBs with differing preloads and compares their performance to a hybrid hydrostatic bearing (HHB). First, design

simulations are conducted using the XLTRC^{TM} Rotordynamics Suite (XLTRC^{2}) [9]. By varying specific design parameters that affect the load capacity of the bearing, it is thought that the lift-off performance of the bearing will also be affected. After the design is completed, the designed FPBs are manufactured and tested. An HHB is also tested for comparison. Lift-off is determined from a shaft circuit voltage and verified with waterfall and shaft centerline plots. All tested bearings are also simulated in XLHydroJet® [10] to determine the validity of predicted results.

2. LITERATURE REVIEW

Early developments of the FPB by Zeidan and Paquette [7, 11] describe the advantages of manufacturing a FPB versus a TPB. Due to their geometry, FPBs eliminate tolerance stack up and pivot wear. There are no pads to install on the bearing thus easing installation. Experiments conducted by De Choudhury et al. [12] demonstrate that, in comparison to a similar five-pad TPB, a FPB operates at a lower temperature and has less frictional power loss.

Since TPBs reduce cross-coupling, FPBs, similar to TPBs in geometry, should also reduce cross-coupling and stabilize the system. Armentrout and Paquette [13] showed that FPBs reduce destabilizing cross-coupling forces. For a four-pad FPB, with L/D = 0.75 at 10,000 rpm, a pad rotational stiffness below 1,000 N-m (113.0 lb-in) yields a bearing with cross-coupled stiffnesses comparable to TPBs. When the pad stiffness is above 100,000 N-m (11,300 lb-in), a FPB acts like a fixed geometry bearing. This leads to destabilizing cross-coupled stiffnesses. Evaluation of the pad web stresses showed that, for an appropriately chosen geometry, the stresses on the pad web are too small to degrade the lifetime due to fatigue.

Models

The physical modeling of FPBs is necessary for predicting their behavior in operation. Early linear models of the bearing dynamic force coefficients by Chen [3] confirmed the stability of a FPB. The method demonstrates that the support web must be thick enough to carry the applied load and avoid fatigue, while at the same time being flexible enough to mimic a TPB. San Andrés [8] introduced a bulk turbulent flow thermal analysis of FPBs, specifically for cryogenic applications. The model shows a reduced whirl frequency ratio (WFR) without loss in load capacity or reduction in direct stiffness or damping. WFR is the ratio between the rotor natural frequency and the onset speed of instability [1], and a lower WFR denotes a more stable bearing.

Effect of Varying Preload

An exact definition of preload, bearing clearance, and pad clearance can be found in the Bearing Design section of this thesis. Elwell and Findlay [14] explored the relationship between load capacity and bearing clearance in TPBs. Since preload is related to bearing clearance, preload is also varied. Results for a laminar, incompressible flow numerical solution of the Reynolds equation yield some insight into the behavior of TPBs. They show that bearing load capacity increases with reduced bearing clearance. However, the pad clearance seems to have little effect on the bearing load capacity [14].

Others who conducted tests over a range of preloads include Wygant, et al. [15]. Their measurements indicated that preload does affect operating eccentricity but not attitude angle. Operating eccentricity is the equilibrium position of the shaft in the bearing for a fixed load, and attitude angle is the angle made by the center of the shaft with respect to the center of the bearing [1].

Lift-off Testing

Scharrer et al. [16] conducted lift-off tests for hydrostatic bearings. These lift-off experiments tested a hydrostatic journal bearing in a liquid nitrogen environment. Several different bearings were used in testing, but the most common geometry is provided in Table 1. The clearance ratio is a description of the bearing clearances as a fraction of the total bearing radius. An exact definition of these terms is provided in the Bearing Design section.

Table 1 Bearing geometry from Scharrer et al. [16]

Diameter	76.2 mm (3.0 in)
Length	31.75 mm (1.25 in)
Recesses	6
Clearance ratio (C_b/R_b)	0.0267

For these tests, Scharrer et al. [16] state that the reversal in shaft direction of rotation from clockwise to counter-clockwise indicates the beginning of hydrodynamic lift-off, as demonstrated in Fig. 3.

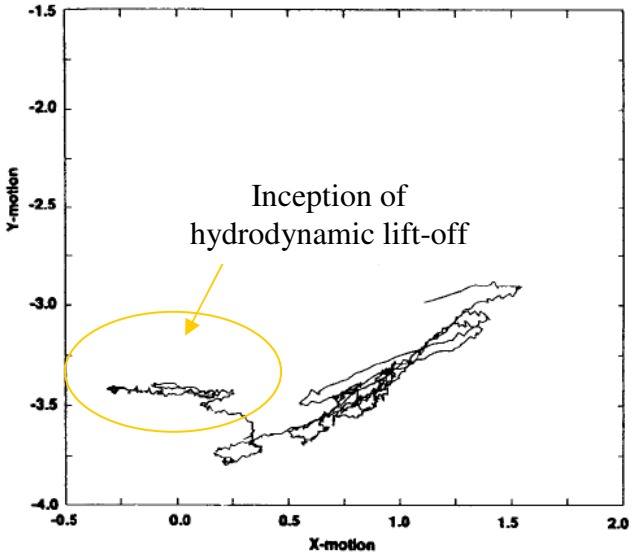

Fig. 3 Hydrodynamic lift-off from Scharrer et al. [16].

Zhu [17] performed tests for Rayleigh step gas bearings using waterfall plots to identify the point after lift-off occurred. In gas bearings, metal to metal contact causes chattering frequencies to develop which can be identified with waterfall plots. The point where these chattering frequencies stop is the lift-off point. An example from Zhu's work can be seen in Fig. 4.

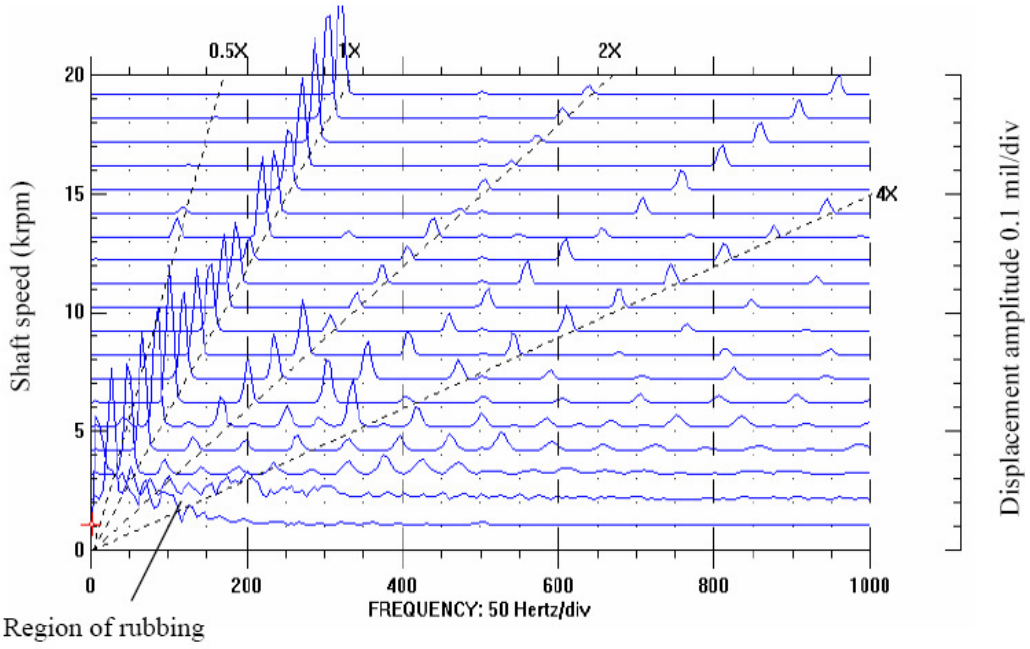

Fig. 4 Gas bearing chattering frequencies indicating rub [17].

Lu and Khonsari [18] used the Stribeck curve for the coefficient of friction to predict lift-off in a constant-radius journal bearing. The bearing had an $L/D = 1$, $C_b/R_b = 0.0138$. The unit load was varied between 3.5 bar and 14.2 bar. With SAE 30 oil, they predicted that increasing unit load generally increased lift-off speed. Reducing the fluid viscosity by heating the oil also increased lift-off speed.

The rubbing that occurs before lift-off can cause wear. Bouyer et al. [19] experimented by running 2,000 start and stop cycles on a two-lobe hydrodynamic bearing. The tests subjected the bearing surface to observable physical wear. However, the study found that despite the wear, the bearing still functioned without observable problems.

3. BEARING DESIGN

The first step in the design of the bearing was to determine which parameter had the most significant effect on lift-off. The simulations do not predict lift-off. Instead, they calculate the film thickness developed in the bearing. For the design simulations, the maximum load capacity of the bearing is defined to be the load where the minimum film thickness is equal to twice the surface roughness of the rotor. At this point, rubbing is assumed to occur between the rotor and bearing. For a typical turning manufacturing process, the surface roughness is approximately 2 μm (0.08 mils) [20]. Using these definitions, both preload and offset are varied to discover their effect on bearing load capacity. This definition is used in all the simulations to determine the load capacity.

Bearing preload is a ratio that compares the bearing radius, the shaft radius, and the pad radius using specific clearances. These radii and clearances are defined in Fig. 5.

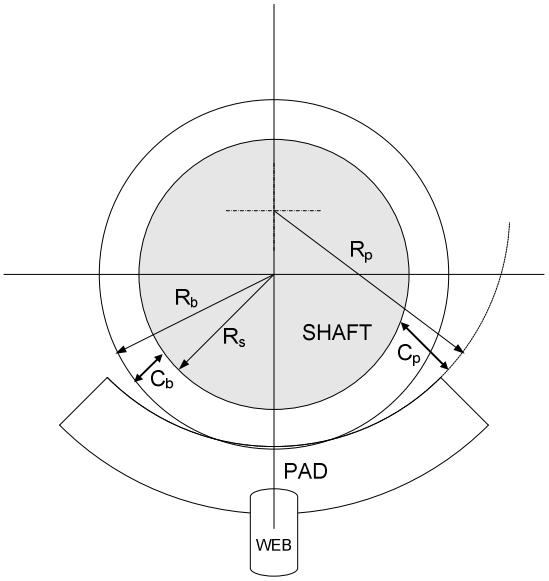

Fig. 5 Definition of rotor-bearing system radii [1].

To adjust bearing preload, the radial bearing clearance, C_b, is altered according to Eq. 2 from San Andrés [1], where m is the bearing preload,

$$m = 1 - \frac{C_b}{C_p}. \tag{2}$$

The following relationships describe the clearances:

$$C_b = R_b - R_s, \tag{3}$$

$$C_p = R_p - R_s. \tag{4}$$

Bearing offset is also varied to see its effect on maximum load capacity. Offset is defined by the Eq. 5, where α is the pivot or web offset:

$$\alpha = \frac{\theta_p}{\beta}. \tag{5}$$

The angles used in this relationship can be seen in Fig. 6.

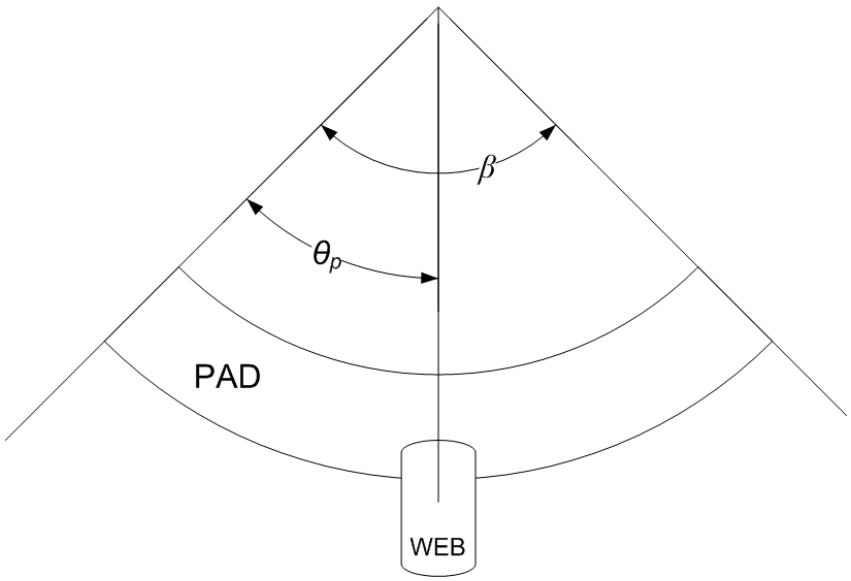

Fig. 6 Definition of web offset [1].

Eccentricity ratio is determined by the rotor displacement from the center of the bearing housing (in the x-y plane). The dimensional eccentricity is defined as:

$$\varepsilon = \sqrt{e_x^2 + e_y^2}, \tag{6}$$

and the eccentricity ratio is

$$\varepsilon_0 = \frac{\varepsilon}{C_b}. \quad (7)$$

The bearing clearance, C_b, is the minimum clearance where contact could occur. Thus a ratio equal to one would refer to contact with the bearing surface, and a ratio equal to zero would be a perfectly centered bearing.

To determine which parameter, preload or offset, has more effect on the rotor-bearing system, simulations are run using the XLTRC^2© bearing program, XLTFPBrg^{TM}. Table 2 shows the design parameters entered into the simulation with a load-between-pad (LBP) orientation.

Table 2 Parameters for the flexure pivot pad support bearing predictions

Parameter	Value	SI Unit	Value	Eng Unit
Rotor diameter	38.1	mm	1.5	in
Bearing axial length	38.1	mm	1.5	in
C_p	106	μm	4.17	mils
C_b	63.5	μm	2.5	mils
Number of pads	5	--	5	--
Pad arc length	58	deg	58	deg
Pad pivot offset	0.5	--	0.5	--
Pad inertia	1.21	μkg-m^2	0.01	lb-in^2
Rotational web stiffness	100	N-m/rad	778	lb-in/rad
Pad damping	0	N-s-m/rad	0	lb-s-in/rad
Supply pressure	0.101	MPa	14.5	psi
Supply temperature	40	°C	106	°F
Load orientation	LBP	--	LBP	--
Material	Bronze	--	Bronze	--

Each parameter was selected by considering a variety of factors. The rotor and bearing geometry and material were determined using the existing bearing housing designed by Dyck [21]. A finite element simulation in Solidworks© determined pad inertia and is available in the Appendix.

The selected pad stiffness came from the recommended pad rotational stiffness of 1.13 – 11,300 N-m/rad (10 – 100,000 lb-in/rad) set forth by Kepple et al. [5]. They used a 50.89 mm (2.0035 in) diameter bearing with $C_b/R_b = 0.00175$. The proposed bearing has a diameter of 38.23 mm (1.505 in) with $C_b/R_b = 0.00333$. The difference in these bearings is small so using a moderate pad rotational stiffness within this range should be acceptable. If the pad stiffness exceeds the recommended upper limit, the web no longer deflects enough for the bearing to behave as a TPB, and the cross-coupled stiffnesses increase significantly. Selecting a lower stiffness further decreases the possibility of instabilities due to cross coupling.

The clearances were selected by choosing a specific preload and offset. The number of pads, pad stiffness, and load orientation were also varied slightly to see their effect on the system. These results will be discussed after noting the effect of preload and offset.

The properties of water are listed in Table 3 with the temperature-viscosity coefficient, φ, defined as follows:

$$\mu_1 = \mu_2 e^{-\varphi(T_1 - T_2)} . \tag{8}$$

This temperature-viscosity coefficient is a variable specific to XLTRC^2©, allowing the program to determine how viscosity varies with temperature. Two reference temperatures (T_1 and T_2) with known viscosities are used to calculate this coefficient.

Table 3 Properties of water at supply temperature = 104 °F (40 °C)

Parameter	Value	SI Unit	Value	Eng Unit
Viscosity at Supply Temp.	653.0	μPa-s	0.64	cp
Density at Supply Temp.	1032	kg/m^3	61.9	lbm/ft^3
Compressibility	459.90	μm^2/N	3.40	mil^2/lb
Specific Heat	4186	J/(kg-K)	0.9989	BTU/(lb-^{o}F)
Thermal Conductivity	0.675	W/(m-K)	0.3656	BTU/(ft-hr-^{o}F)
Coeff. Thermal Expansion	0.00025	1/K	0.000141	1 / ^{o}F
Temp-Viscosity Coeff.	0.014	1/K	0.01017	1 / ^{o}F

Effect of Preload and Offset

When preload is changed, the clearances in the bearing change, affecting the behavior of the fluid film. Since this fluid film supports the bearing, the load capacity of the bearing should also be affected by changes in the preload. Typical values of preload range from 0.2 to 0.6. Beyond 0.6, San Andrés [1] found that frictional losses are high, rendering the bearing impractical.

The bearing simulated in XLTRC^2 gives the changes in maximum load capacity due to changes in preload, shown in Fig. 7. The eccentricity ratio, which is determined by the simulations does not necessarily stay constant as it depends on C_p which changes with different preloads. For details on the bearing used in these simulations, see Table 2 and Table 3. A design running speed of 3000 revolutions per minute (rpm) was selected for the predictions. Also, the unit load capacity, W_{unit}, is defined as:

$$W_{unit} = \frac{W}{LD}. \tag{9}$$

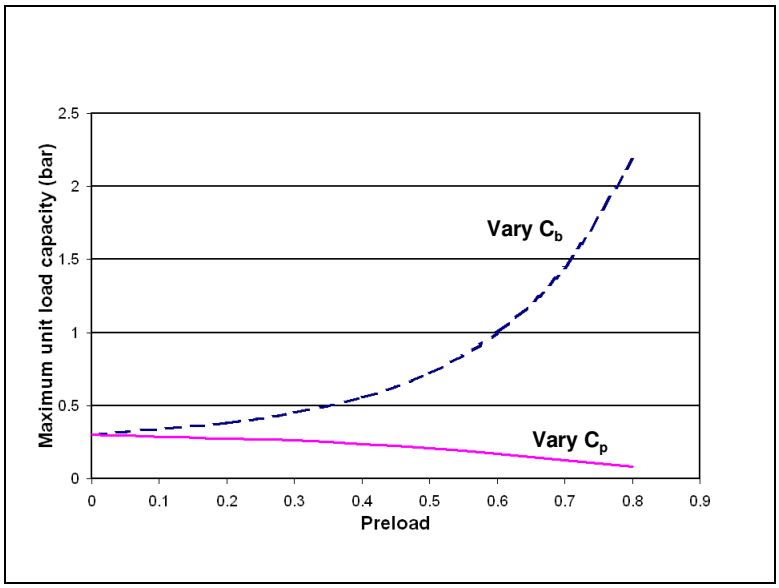

Fig. 7 Predicted maximum load unit capacity for varying preloads at 3000 rpm.

Two different methods of varying preload were conducted, as shown in Fig. 7. The purpose of this figure is to illustrate that changing the preload does change the load capacity of the bearing. The first method for illustrating a changing load capacity holds C_p constant and varies C_b. This moves the entire pad closer to the rotor, changing the preload. The predicted results for this method shown with a dotted line indicate that load capacity increases quickly with increasing preload. Trends simulated by Elwell and Findlay [14] agree with this result—a smaller C_b yields a greater load capacity.

The other method holds C_b constant and varies C_p. This changes the curvature of the pad in order to change preload. Since C_b determines the minimum bearing clearance, changing C_p is more practical from a manufacturing standpoint. Each FPB will be compared to a HHB with no preload. The FPB must also have the same minimum clearance, or C_b, as the HHB. To change preload for the different FPBs, then, C_p will be changed. As shown in the solid line in Fig. 7, the maximum load capacity decreases gradually when increasing preload in this manner. Elwell and Findlay [14] found no effect on the load capacity for an increasing C_p.

Next, the web offset is varied in XLTRC^2© at 3000 rpm with $m = 0.5$. The clearances used for varying offset and for changing other parameters are as follows: C_b = 63.5 μm (2.5 mils) and C_p = 127 μm (5 mils). These clearances used for the simulations in Fig. 8 to Fig. 12. The results for varying offset are shown in Fig. 8.

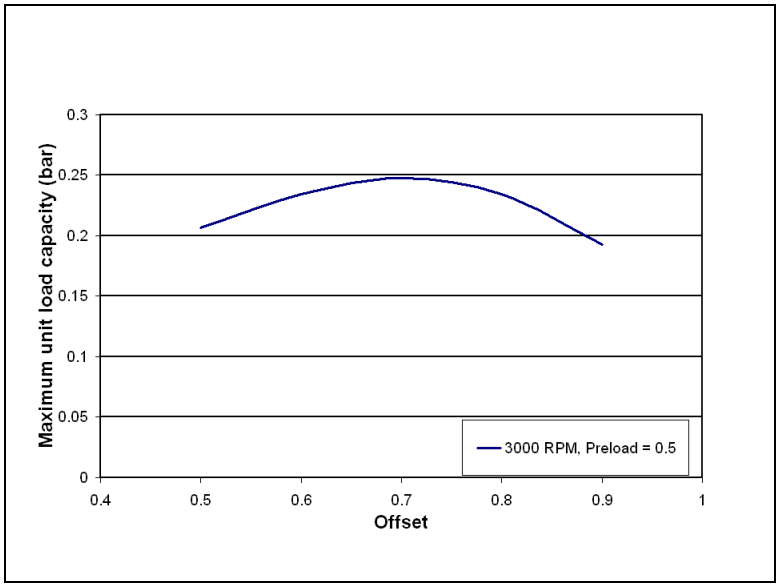

Fig. 8 Predicted maximum unit load capacity for varying offsets.

As the offset increases, the maximum load capacity also increases. However, this value peaks at relatively small value. The total change in load capacity is significantly less for a varying offset than for a varying preload. Thus, for reasonable ranges in both preload and offset, changing the preload would have more effect on the load capacity of the bearing than changing the offset. This is true regardless of the way the preload is varied.

Drag Torque and Power Loss

To evaluate the drag torque that is caused by the FPB support bearing, XLTFPBrg^{TM} is again used to predict the power loss at various shaft speeds. From the power loss, the drag torque is calculated using a 53 N (12 lb_f) load. This prediction was made prior to receiving any bearings. Later shaft weight measurements resulted in a load of 31.1 N (7 lb_f), so this prediction should give a reasonable, conservative approximation. The results are shown in Fig. 9.

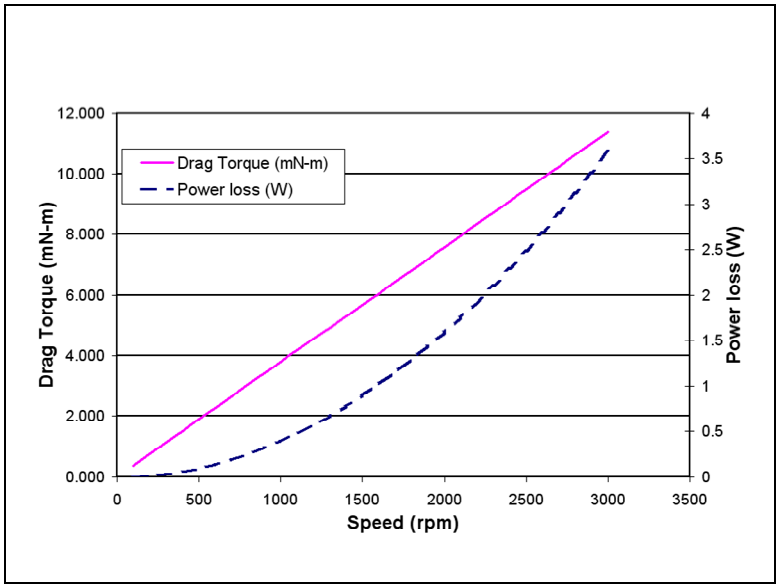

Fig. 9 Predicted power loss and drag torque for a FPB speed ramp up to 3000 rpm (m = 0.5, θ_p = 0.5).

Generally, the power loss grows along a second order curve while the drag torque appears linear with speed. Both the power loss and drag torque are very small up to the maximum design speed, 3000 rpm.

Other Design Considerations

For the previous simulations, certain design choices were made to consider the effect of preload and offset. However, there are other parameters that affect maximum load capacity. Varying the number of pads can also change the load capacity, as shown Fig. 10.

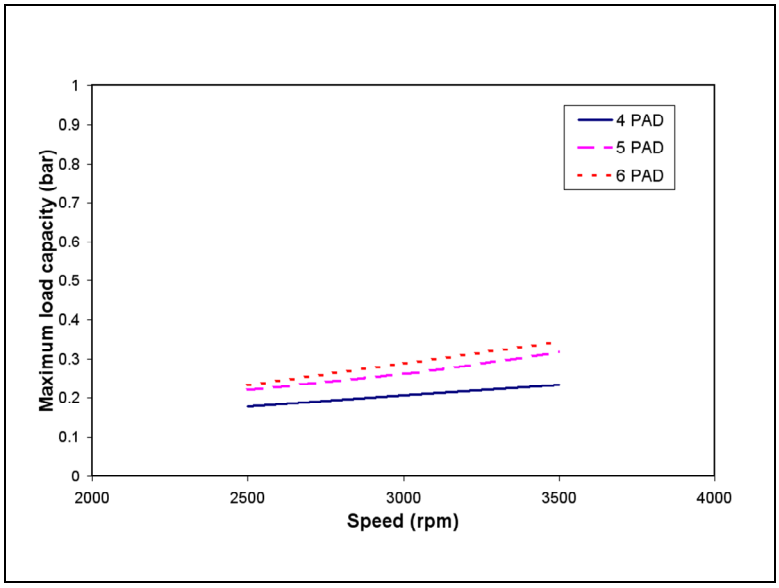

Fig. 10 Maximum unit load capacity for varying number of pads at 2500, 3000, and 3500 rpm (m = 0.5, θ_p = 0.5).

Near the maximum design speed, the six-pad configuration has the highest unit load capacity. However, increasing the number of pads also increases the manufacturing cost. A five-pad configuration would not be easily split in two. Although it is not necessary to split the bearing for these tests, using a bearing that would more likely be used in real industry applications is preferable to something that would not be considered. Therefore, the four-pad configuration will be used in the bearing.

Next, the load configuration is simulated. For the four-pad configuration, the load is set to either LBP or load-on-pad (LOP), and the results are shown in Fig. 11.

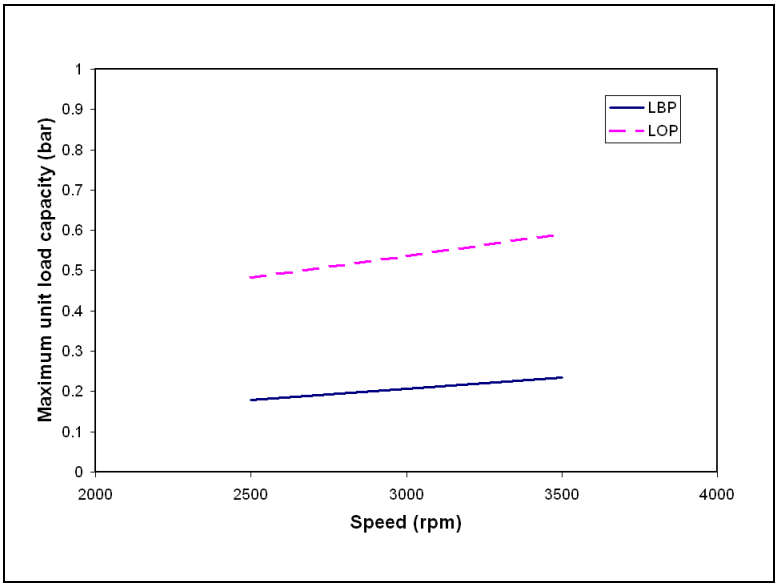

Fig. 11 Maximum unit load capacity for varying load configuration at 2500, 3000, and 3500 rpm (m = 0.5, θ_p = 0.5).

The predictions show that the LOP configuration gives a much larger load capacity. However, LOP is generally used for lightly loaded high speed applications; whereas, LBP is used for more heavily loaded applications [1]. Thus, the LBP configuration is chosen because the magnitude of the applied loads in the experimental tests could be very large.

Finally, the effect of pad rotational stiffness is evaluated for a four-pad FPB. The low stiffness refers to the stiffness given by Table 2, and the high stiffness is ten times the table value. As can be seen in Fig. 12, pad stiffness increases the load capacity slightly. Simulations showed that, in general, larger rotational stiffness led to larger magnitude cross-coupled stiffnesses. Thus, it is desirable to operate at lower rotational stiffnesses. A low rotational stiffness will be chosen for manufacture, and this parameter will not be varied.

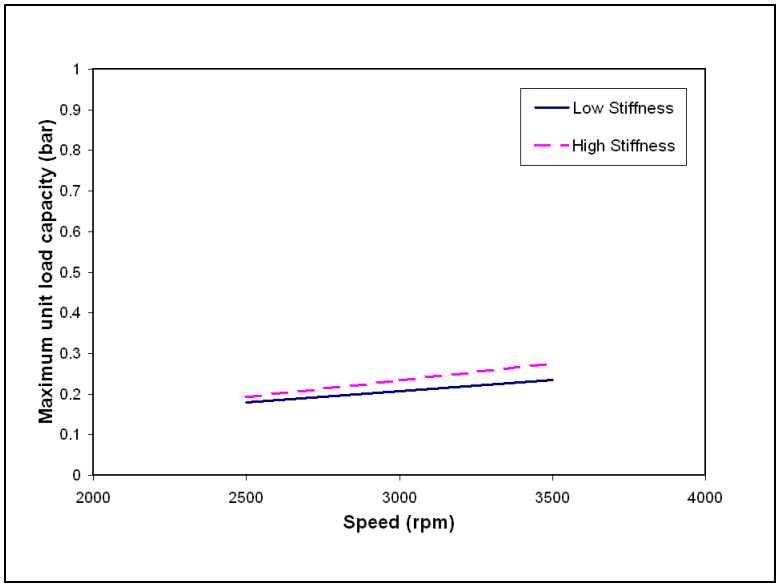

Fig. 12 Maximum unit load capacity for varying pad rotational stiffness at 2500, 3000, and 3500 rpm (m = 0.5, θ_p = 0.5).

Test Bearings

According to the previous simulated results, changing the preload does change the load capacity of the bearing. Zero preload is the best preload for the method of varying C_p, according to Fig. 7. However, three preloads are selected. A bearing with no preload would be best for comparison, but that was not selected for this study. Future studies might explore the effect of changing C_p to change load capacity.

Having determined the effect of preload and offset, three different preload bearings were manufactured for experimental testing. The designed bearing geometries can be found in Table 4.

Table 4 Designed FPBs

Preload	0.3	0.5	0.7	Unit
Radial axial length	38.1 (1.5)	38.1 (1.5)	38.1 (1.5)	mm (in)
C_p	90.71 (3.57)	127.00 (5.00)	211.67 (8.33)	μm (mils)
C_b	63.5 (2.50)	63.5 (2.50)	63.5 (2.50)	μm (mils)
Offset	0.5	0.5	0.5	
Number of pads	4	4	4	--
Pad arc length	72	72	72	deg
Pad pivot offset	0.5	0.5	0.5	--
Material	660 bearing bronze	660 bearing bronze	660 bearing bronze	

The web design for these bearings was performed by the manufacturer since it is a patented design. However, an approximate design of the web can be found in the Appendix. Two views of the m = 0.3 bearing design are shown in Fig. 13 and Fig. 14.

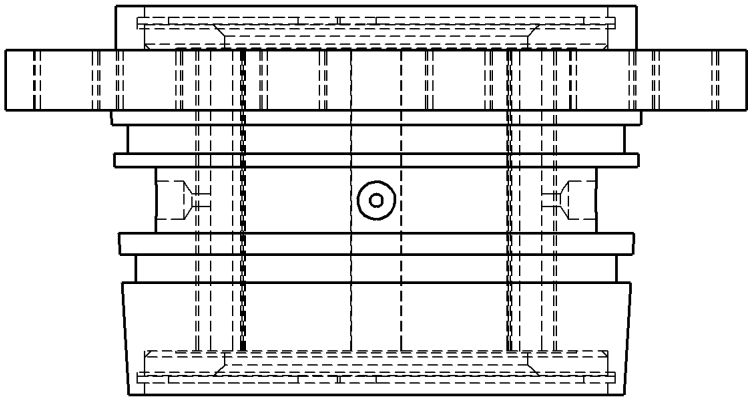

Fig. 13 FPB top view (m = 0.3), bearing diameter 38.23 mm (1.505 in.).

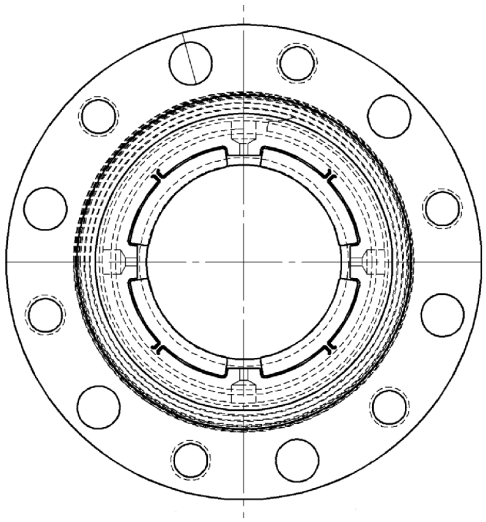

Fig. 14 FPB front view (*m* = 0.3), bearing diameter 38.23 mm (1.505 in.).

The fluid supply is through four inlet ports between the four pads. Also, two end seals help prevent fluid leakage in the axial direction. These features are shown in Fig. 15.

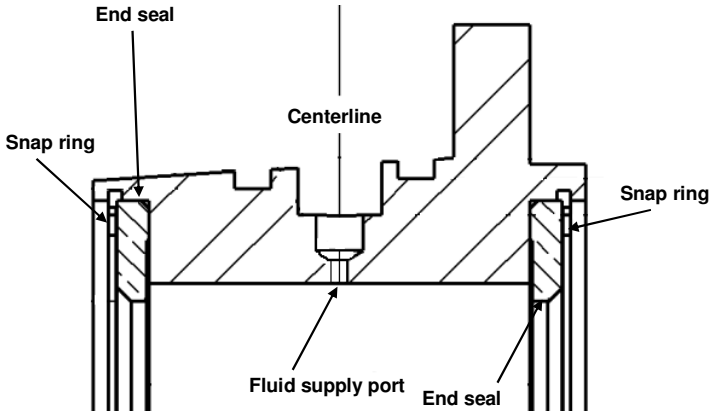

Fig. 15 FPB section view showing end seals and supply ports, pad length between seals = 38.1 mm (1.5 in).

During testing of the FPBs, the fluid supply pressure was varied. Three different fluid supply pressures were used with different flowrates. These supply pressures and corresponding flowrates are shown in Table 5.

Table 5 Supply pressures and flowrates for FPB testing

Supply pressure (bar)	Flowrate (lpm)
0.69 (10 psia)	5.68 (1.5 gpm)
2.76 (40 psia)	10.22 (2.7 gpm)
5.52 (80 psia)	13.63 (3.6 gpm)

In addition, one six pocket HHB was manufactured for comparison with FPBs, and its details can be found in Table 6.

Table 6 HHB geometry

Parameter	Value	Unit
Bearing axial length	38.1 (1.5)	mm (in)
Radial bearing clearance	63.5 (2.50)	μm (mils)
Number of pockets	6	--
Pocket axial length	11.97 (0.47)	mm (in)
Pocket depth	406 (16)	μm (mils)
Orifice diameter	1.397 (0.055)	mm (in)
Orifice location relative to pocket (%)	50	--
Material	660 Bearing Bronze	--

The outer design of the HHB is similar to the FPB but does not contain any end seals. The geometry and six pockets or recesses of the HHB can be seen in Fig. 16. The fluid supply pressure for the HHB was varied linearly with time to match a linear speed profile. Details about this pressure profile are provided in the Results section of this thesis.

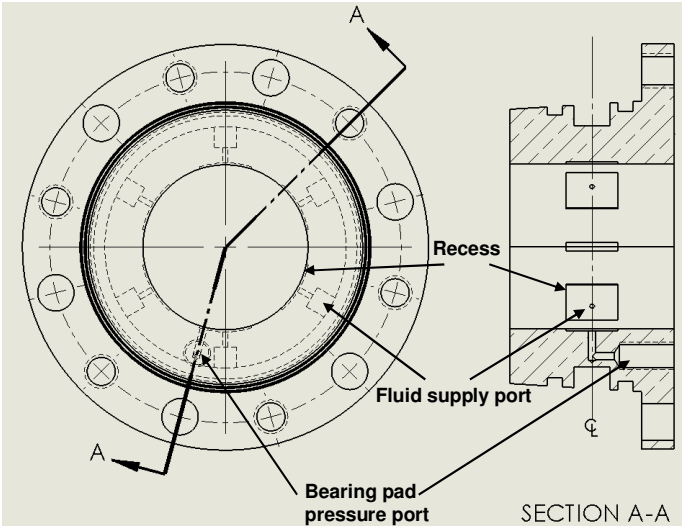

Fig. 16 HHB geometry with supply ports and recesses shown.

While Fig. 16 gives a general view, the detailed pocket or recess geometry is shown in Fig. 17. The recess has a uniform depth, creating no curvature in the recess. Thus, the diameter of the recess and the diameter of the bearing are concentric. If a fictitious pad were created with the geometry of the pad, the bearing would have no preload. Pictures of both of these bearings are included in Fig. 18 and Fig. 19.

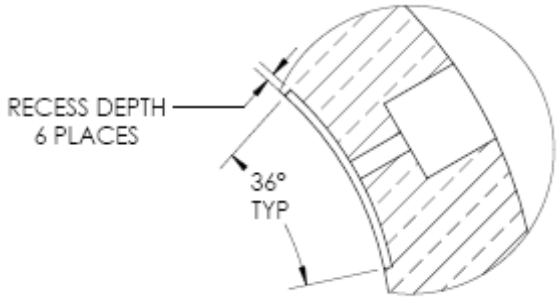

Fig. 17 HHB recess or pocket detail, depth = 483 µm (19.0 mils).

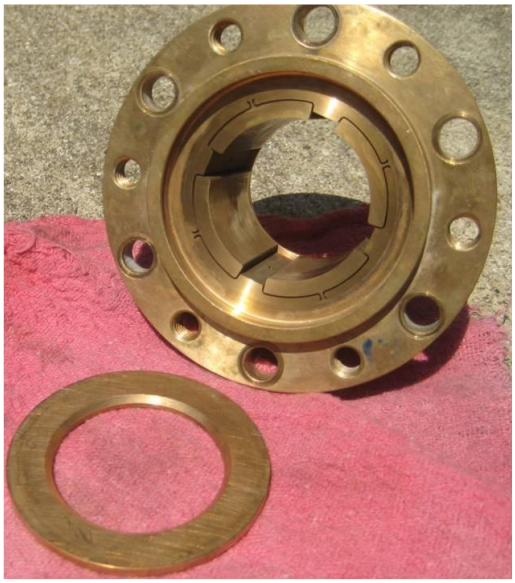

Fig. 18 FPB with seal end removed (660 bearing bronze, *m* = 0.3 design).

Fig. 19 Photo of HHB made from 660 bearing bronze.

4. EXPERIMENTAL PROCEDURE

With the bearing design and specification complete, the next step is to test the bearings. The test rig used for performing bearing tests is shown in Fig. 20.

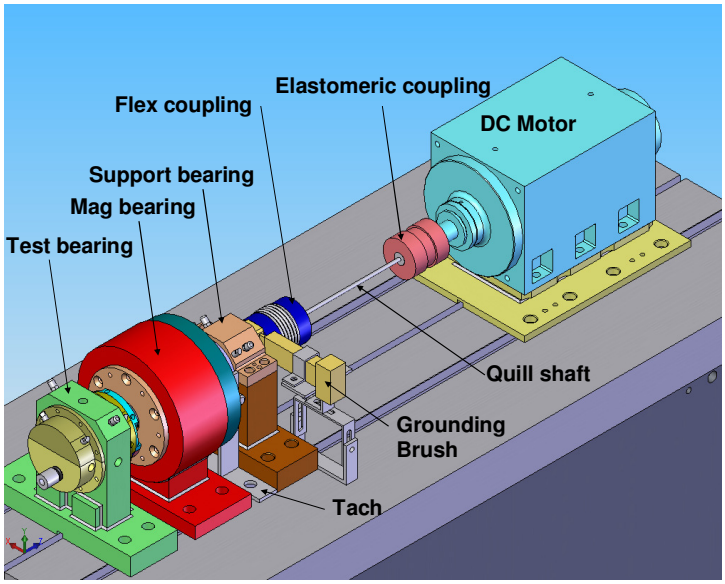

Fig. 20 Schematic of test rig.

A DC motor turns the shaft supported on one end by roller element bearings and on the other end by the test bearing. The test bearing lubricant exits into the enclosure surrounding the test bearing. A magnetic bearing with a radial clearance of approximately 508 microns (20 mils) applies shaft load. However, it does not support the shaft during testing. The shaft contacts at a grounding brush for use in the shaft circuit described later, and the tachometer measures the rotational shaft speed. A large protective cage encloses the entire test rig as shown in Fig. 21.

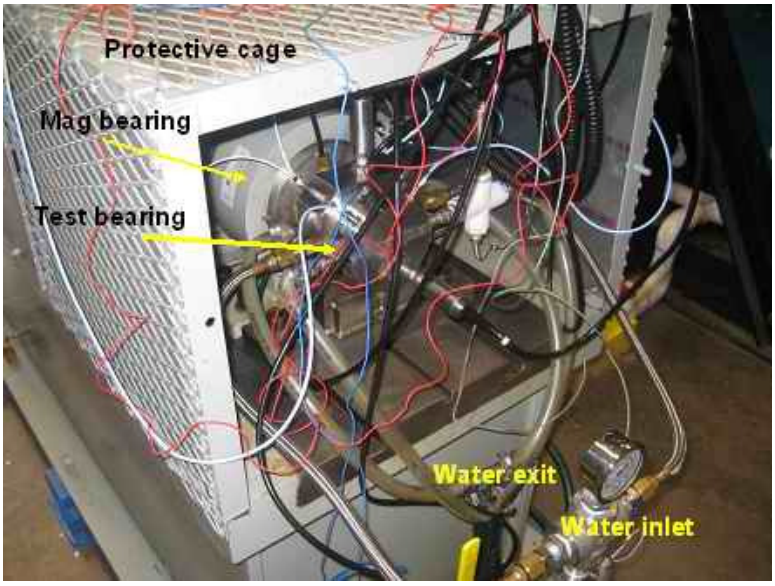

Fig. 21 Photo of front of test rig.

For testing, a circuit runs through the shaft with contacts at the test bearing and the grounding brush. When the shaft disconnects from the surface of the test bearing, the circuit breaks. In this manner, the circuit determines shaft lift-off. Further detail of this circuit and the test rig design is displayed in the schematic in Fig. 22.

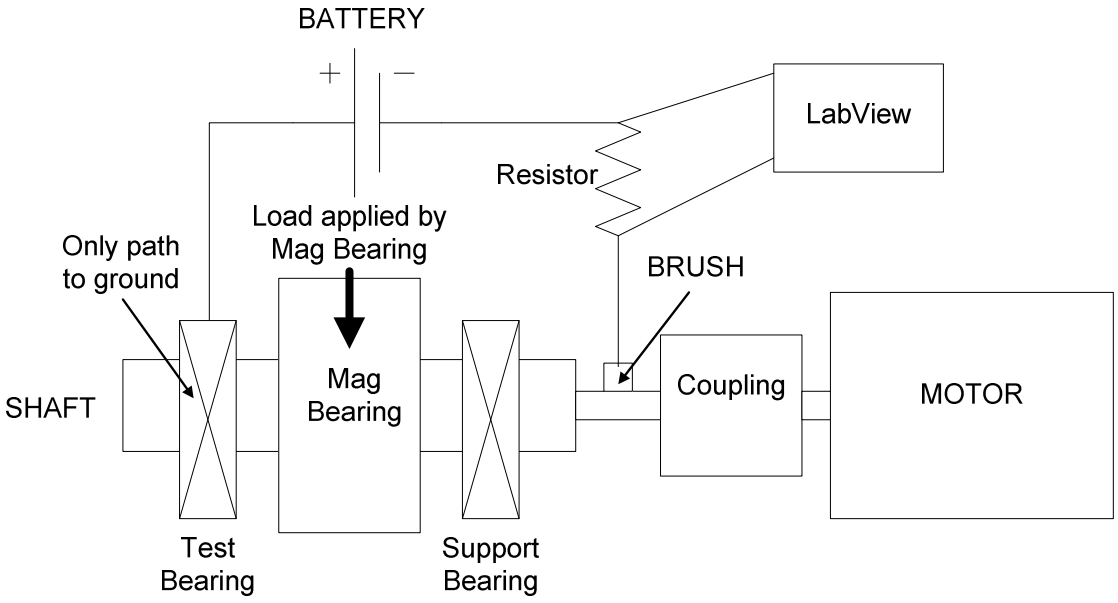

Fig. 22 Shaft circuit schematic showing load and ground.

The support bearings, magnetic bearing, and coupling are all electrically insulated. The support bearings are silicon nitride roller-element type bearings but do not pass any current. No contact is made at the magnetic bearing due to its large clearance with the shaft. The coupling is an elastomeric type that does not allow current flow. Hence, the current will pass from the battery through a resistor into the test bearing. From there, it will enter the shaft and then exit through a brush at the other end of the shaft. Variations in voltage across the resistor will be monitored and recorded in LabView® to determine the exact moment of lift-off when the circuit is broken.

The shaft circuit voltage determines lift-off, but a variety of instrumentation obtains supporting data. Proximity probes determine shaft position at three different locations. Pressure and temperature probes record the test operating conditions. The motor controller sends LabView® the motor speed. In addition, accelerometers at the test bearing, support bearing, and motor record vibration data.

The procedure listed below shows a step-by-step process for lift-off testing. The first part of this procedure deals with bearing alignment. The second part gives the test procedure.

Bearing Alignment Procedure

1) Install bearing into the test pedestal by tightening the insertion bolts all the way in.
2) Loosen the insertion bolts and insert 50.8 μm (2.0 mil) shims at four positions on the bearing (on the pad if applicable). Note that the magnitude of shimming depends on bearing clearance.
3) Tighten bolts and lock bearing with locking bolts.
4) Measure depth with a micrometer-type depth gauge at three points around the bearing face to ensure there is no cocking of the bearing in the test pedestal. The depth at each of these three points should be within 12.7 μm (0.5 mil) of each other.
5) Remove the shims from between the shaft and the bearing.
6) Close the test bearing pedestal with the outer housing and install proximity probes to proper depth.
7) Energize the magnetic bearing and enter calibration factors for loading.
8) While recording bearing position data in LabView®, load the shaft in a manner to bump it against the bearing surface. Repeat these bump tests in every direction until a clear picture of the bearing clearance is formed.
9) Determine bearing clearance from the bump test data in both the *X* and *Y* directions.
10) The bearing alignment is complete if the *X* and *Y* calculated clearances are within 25.4 μm (1 mil) of each other. This ensures the shaft is centered and can move freely.

Test Procedure

1) Turn on the pump to buffer water to the test bearing.
2) Turn on air to the air seal that prevents water flowing axially to the magnetic bearing.

3) Establish a flow of water to the bearing based on the supply pressure specified by the test case. The test matrix showing all test cases is shown in the Appendix.
4) Begin LabView® data acquisition.
5) Turn on the motor and accelerate to the design speed with the load and pressure profile given by the specific test case.
6) Record data to both a binary file and a spreadsheet.
7) Stop the motor and repeat each test case until 10 iterations of current test case are completed.
8) Proceed to next test case. If all test cases are complete for current bearing, turn off water and repeat bump test as described in the bearing alignment procedure. This will determine if the bearing has moved substantially during testing.
9) Remove current bearing and observe wear.
10) Proceed to next bearing and repeat bearing alignment procedure and test procedure.

Bearing Clearance Measurement

In FPBs, the bearing clearance (C_b) is the minimum clearance in the bearing, thus it will be used to determine bearing eccentricity and preload. Typically, one could place the shaft in contact with the center of one pad and then move it to the center of the opposing pad to determine bearing clearance from the displacement. However, due to the setup of the test rig, the test bearing could only be mounted in the LBP position. This prevented a simple shaft up and down bump test to determine bearing clearance. Loading the shaft at a 45° angle to attempt load-on-pad proved unmanageable for determining bearing clearance. When load was applied at an angle, the shaft slipped off the pad to one of the LBP pad positions.

Instead of trying to load directly on the pad, bump tests were performed over the bearing circumference for eight different load directions. Loads covered the horizontal, vertical, and 45° diagonals in the bearing. An example of the resulting data is shown in Fig. 23.

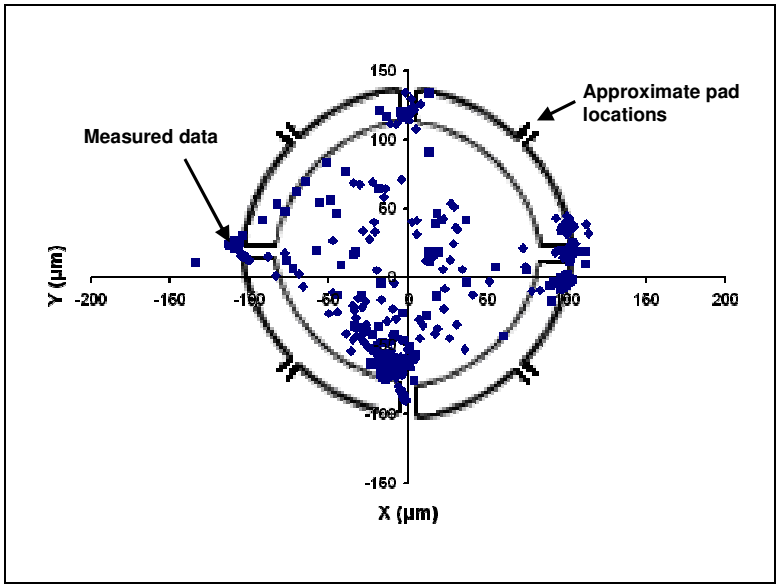

Fig. 23 Shaft centerline bump test data, FPB (Designed *m* = 0.3).

There is a concentration of data points at the four corners between the pads. Notice also that there are points along the pads in between these four corners. The four arrows indicate the web or center locations of each of the four pads. Clearly, the shaft has the greatest displacement in between the pads. Using this data, a bearing clearance circle can be drawn such that it touches the most likely location of the center of each of the four pads. After centering the bearing at point (0,0), the bearing clearance circle appears as shown in Fig. 24.

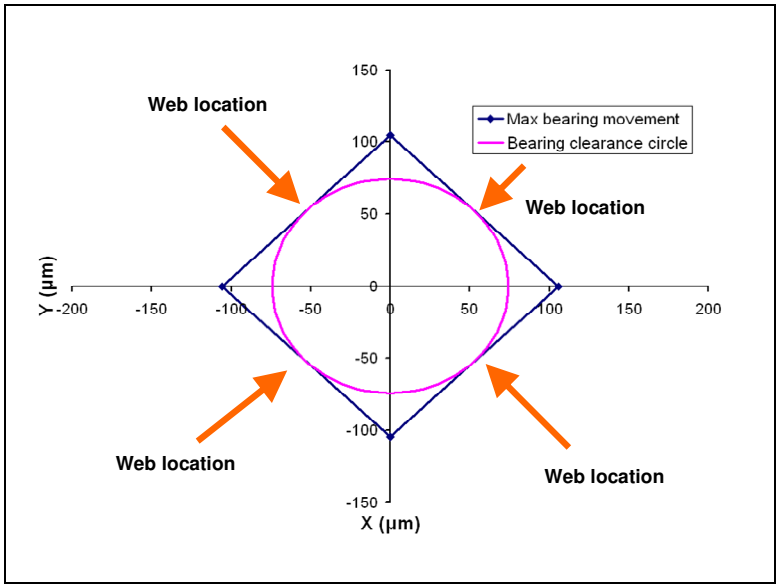

Fig. 24 Clearance circle FPB (Designed m = 0.3).

This method is repeated to obtain average radial bearing clearance values for each bearing. A summary of the average bearing clearance is in Table 7.

Table 7 Measured average C_b

Designed preload	Designed C_b µm (mils)	Measured C_b µm (mils)
0.3	63.5 (2.5)	74.42 (2.93)
0.5	63.5 (2.5)	60.71 (2.39)
0.7	63.5 (2.5)	66.55 (2.62)

The manufactured C_p and C_b are shown in Table 8.

Table 8 Manufactured clearances with tolerances

Preload	Manufactured C_b µm (mils)	Manufactured C_p µm (mils)
0.3	57.15-63.5 (2.25-2.5)	83.82-90.17 (3.30-3.55)
0.5	57.15-63.5 (2.25-2.5)	120.65-127.00 (4.75-5.00)
0.7	57.15-63.5 (2.25-2.5)	208.28-214.63 (8.20-8.45)

Using the upper end of the tolerance range, the difference between C_p and C_b is calculated for the given manufactured clearances. This difference is then used to calculate a new preload for each bearing. A new C_p is calculated by adding this difference to the average measured C_b. From these values, a preload can be calculated according to Eq. 2. The resulting measured preloads and clearances are summarized in Table 9.

Table 9 Summary of measured clearances and preloads for FPBs

Designed preload	Measured C_b µm (mils)	Calculated C_p µm (mils)	New preload
0.3	74.42 (2.93)	101.63 (4.00)	0.27
0.5	60.71 (2.39)	124.21 (4.89)	0.51
0.7	66.55 (2.62)	214.72 (8.45)	0.69

The actual measured C_b for the HHB is different from the value given by the manufacturer. The given C_b is 63.5 ± 2.5 µm (2.5 ± 0.1 mils). However, the measured value according to the procedure determined above was 59.1 µm (2.327 mils). The measured values for the clearances and preloads of all the bearings will be used in the Results section.

Lift-off Determination

There are three methods used in this paper for determining and confirming lift-off. First, the shaft circuit voltage is monitored for disturbances indicating lift-off. This was by far the most successful method. It achieved repeatable results within several hundred rpm. Considering the rapid acceleration of the shaft (0 to 4500 rpm in approximately 0.84s), this is a highly accurate result.

Second, waterfall plots are made of the accelerometer data showing vibrations in the test pedestal. Larger vibration amplitudes are observed during bearing rubbing than when it has lifted off. This second method has been used in air bearings and evaluates

waterfall plots of the displacement data [19]. A chattering frequency at low speeds occurs when there is metal-to-metal contact. This method yielded some accurate results but lacked consistency in testing. The exact point of lift-off was harder to determine due to several different high frequencies to watch during bearing rub.

Finally, since the bearing clearance defines the shaft position relative to the bearing surface, shaft centerline plots can be used to verify lift-off. Centerline plots depend on the definition of the bearing surface. Since there is some uncertainty in determining the bearing clearance, exact lift-off speeds will also have some uncertainty when calculated by this method.

After consideration of the three methods described, the most repeatable and accurate indicator of lift-off comes from variation in the shaft voltage. For the example given in Fig. 25, there is a clear drop of about 0.25 volts as the shaft rises from the bearing housing.

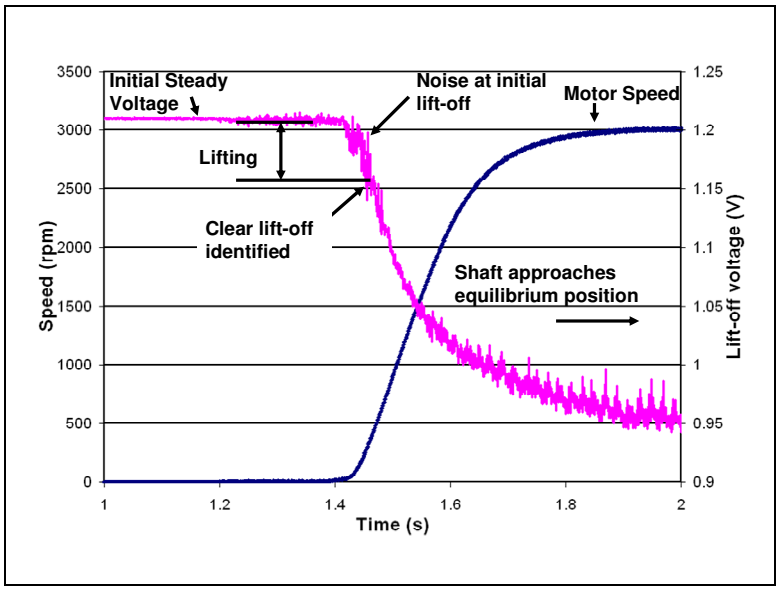

Fig. 25 Lift-off voltage for FPB (*m* = 0.27, 0.689 bar supply, 0.135 bar static unit load, test case 4-12-08).

In this case, there is an initial lift-off with some associated noise as the shaft begins to spin. However, voltage continues to drop, indicating the shaft has fully lifted

off. For practical purposes, lift-off is defined as the point where the average change in voltage from the steady voltage is greater than 0.05 volts. Since the noise in the signal may vary up to a magnitude 0.03 volts, this condition eliminates predicting the wrong lift-off voltage due to noise in the signal. To filter out touchdowns or contacts at the very beginning of the lift-off, this condition must be met for a minimum of 8 ms. The lift-off speed recorded for this particular test case is 460 rpm.

Vibration amplitudes over the range of running speeds can also be used as a method of verifying lift-off. Accelerometers mounted on the test bearing pedestal record these vibrations. The amplitudes of these vibrations are plotted in a waterfall plot in Fig. 26 showing the frequency of the vibration and its running speed.

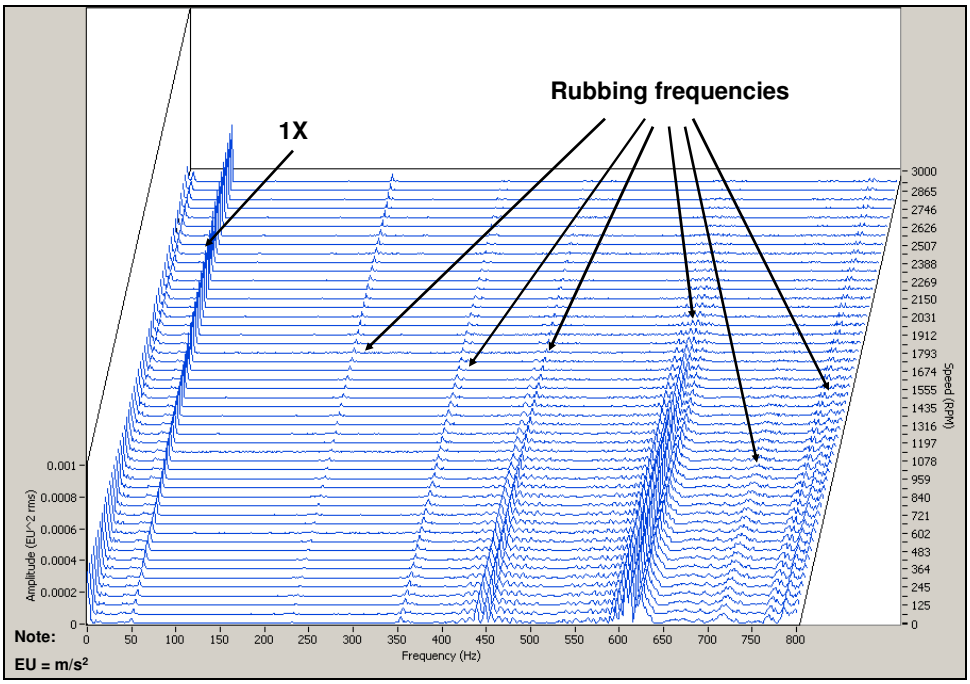

Fig. 26 Waterfall plot of rubbing frequencies (*m* = 0.27, 0.689 bar supply, 0.135 bar static unit load, test case 4-12-08).

The rubbing frequencies are supersynchronous and begin at startup. The amplitudes of vibrations are significantly reduced by the time the shaft reaches 3000 rpm. However, the rub frequency amplitudes do not all fall off at the same running

speed. For example, the vibration closest to the 450 Hz frequency appears to reduce dramatically near 1500 rpm while the 600 Hz frequency does not drop until 2200 rpm. This makes it difficult to predict an exact lift-off speed from these data. When the lift-off voltage technique was used on this same data set, the lift-off speed determined was 460 rpm. This example gives a conflicting result with the lift-off voltage technique, illustrating the difficulty in achieving consistent results with this method.

A better case is shown in Fig. 27. The 600 Hz frequency in this test case shows a drop around 1300 rpm. This is very close to that predicted by the 1380 rpm predicted by the lift-off voltage technique. The reason for the large difference in lift-off rpm between this test case and the one done later (4-12-08) can be attributed to a variety of factors. The $m = 0.27$ bearing was removed in between the tests and the C_b changed slightly. Another factor could be some wear at the bearing surface affecting the lift-off speed. Regardless, this figure is included to show that the rubbing frequency technique does seem to give an accurate range for the resulting lift-off, but it is difficult to determine an exact lift-off speed.

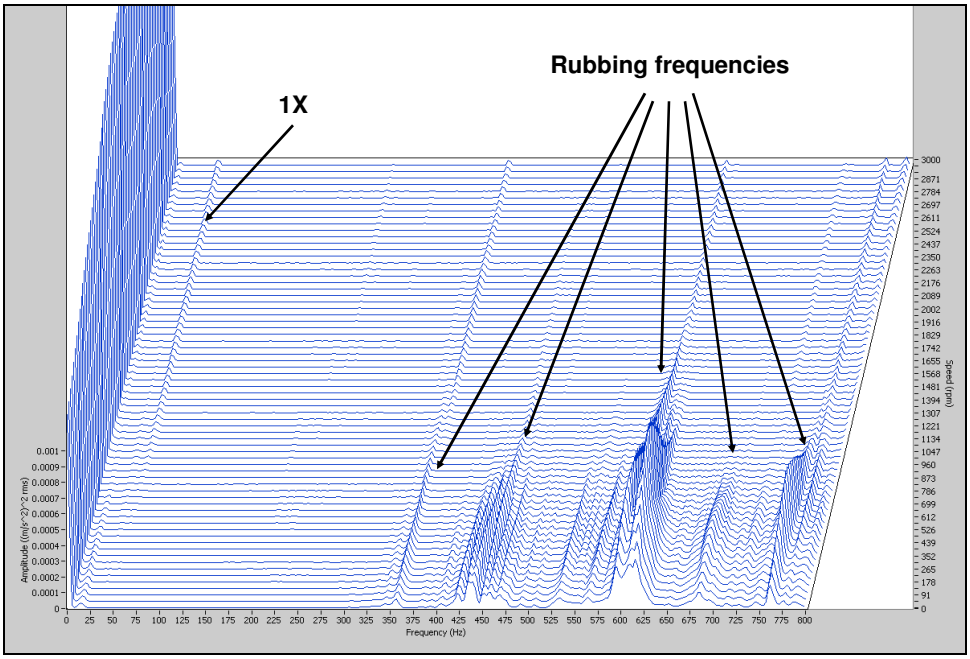

Fig. 27 Waterfall plot of rubbing frequencies (*m* = 0.27, 0.689 bar supply, 0.135 bar static unit load, test case 3-29-08).

The final confirmation of lift-off comes from the proximity probe shaft centerline plots. Continuing with the case in Fig. 25, results for the shaft centerline plot are shown in Fig. 28.

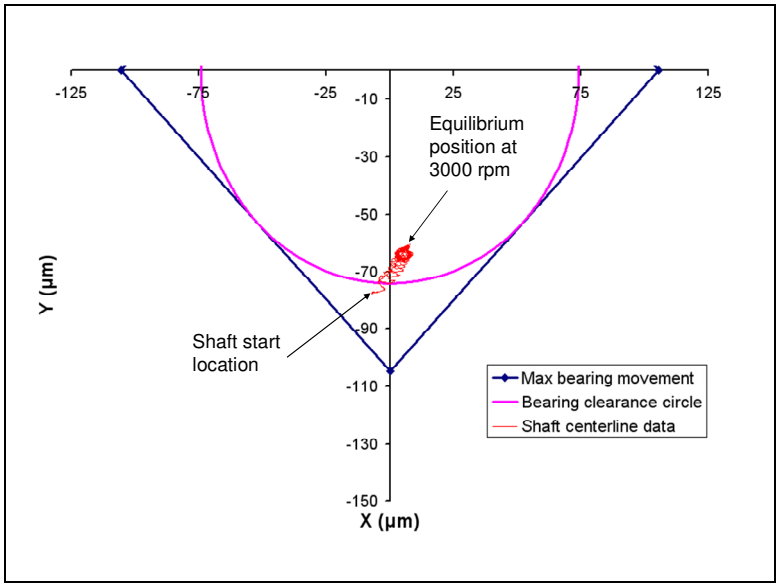

Fig. 28 Shaft centerline movement (*m* = 0.27, 0.689 bar supply, 0.135 bar static unit load, test case 4-12-08).

The shaft centerline plot shows the shaft rotating in a clockwise manner and rising quickly to its equilibrium position at 3000 rpm. The eccentricity ratio calculated with the bearing clearance circle as shown is $\varepsilon_0 = 0.86$. From these data, the shaft clearly lifts off from the bearing surface and achieves an equilibrium position. The problem with determining lift-off speed is that the bearing clearance circle is also ideal. Since the pads can move, determining the exact point where the shaft stops contacting the pad is at best an educated guess. With the bearing clearance circle drawn as above, the shaft centerline plot indicates a lift-off speed of less than 10 rpm, which is quite different from the 460 rpm calculated by the lift-off voltage method. The shaft centerline plot shows clear lift-off, but is not useful for determining the exact lift-off speed.

5. RESULTS

Analyzing test data according to the criteria described in the previous section enables lift-off speeds to be determined. The lift-off speeds for FPBs will be compared to results and predictions for a HHB. Recall that predictions are based on the predicted load capacities of each bearing.

Predictions were made using XLHydrojet®, a rotordynamics program designed for hydrodynamic and hydrostatic bearings. A grid size of 21 circular points by 13 axial points was used, and the code was run until it converged. The program does not calculate lift-off speed directly. Instead, the program predicts eccentricities at specific running speeds based on an inputted load. Using these eccentricity results and knowing the bearing clearance allows one to calculate the fluid film thickness via Eq. 7. When this fluid film thickness falls below 2.0 μm (0.07 mil), which is a typical machined surface roughness, then contact is assumed to occur. Another way to interpret this same limit is to say that when the eccentricity ratio is greater than 0.97, contact occurs. The first speed after the fluid film thickness is greater than the minimum value is the predicted lift-off speed.

A comparison of the lift-off speeds for the FPBs with a simple constant shaft weight load (unit load = 0.135 bar) is shown in Fig. 29. No additional load was applied with the magnetic bearing in this test case.

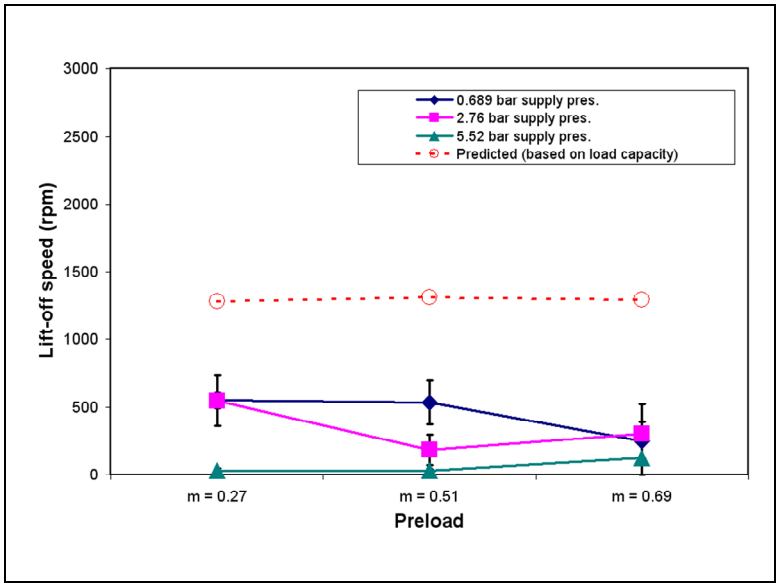

Fig. 29 Lift-off speed comparison for FPB (0.135 bar static unit load due to rotor weight only, varying supply pressure).

In each case, lift-off occurs before 700 rpm. A general trend of decreasing lift-off speed with increasing preload is evident but inconsistent. One standard deviation is shown for ten test runs.

In Fig. 29, the predicted lift-off speeds are much higher than actual recorded speeds. These predicted speed are based on load capacity predictions. It is important to note that the load capacities were predicted at a fixed running speed. The load was then increased until the fluid film thickness fell below the 2.0 μm (0.07 mil) threshold. For the experimental results, the running speed was varied, and the load applied remained constant.

The results in Fig. 29 show that increasing supply pressure reduces the lift-off speed. Lower lift-off speeds correspond to less rubbing on the bearing, thus increasing bearing supply pressure improves lift-off. Hydrodynamic bearings are not designed to operate hydrostatically so this supply pressure dependency was unexpected. One explanation of this pressure effect could be the phenomenon of “hydraulic jack.” That is, the orifice directly below the shaft applies enough pressure to lift the shaft slightly.

This is typically seen in TPBs where the orifice is on the pad. However, this is most likely not happening in the FPB.

Another explanation comes from the restriction of the flow out of the bearing by the end seals in the FPB. The end seals prevent the water from exiting immediately, allowing some pressure development to occur in the "pool" between the pads. The pressure in this pool helps support the shaft and improve the lift-off in the bearing. Practically, however, the lowest pressure that still achieves reasonable hydrodynamic lift-off would be chosen. Hence, for simplicity, the lowest supply pressure of 0.689 bar will be shown in the following test results. Any exceptions to this are noted in the text.

Linearly Increasing Unit Load

The unit load on each bearing was increased linearly during every test case except the shaft weight-only cases. That is, the magnetic bearing applied a force that increased linearly with time. The load started as the shaft began its speed ramp and reached a maximum at the final running speed, called the design speed. Due to the nature of the LabView® Virtual Instrument (VI) that sent the force to the bearing, a force pulse could only be sent once per loop. Thus, loop buffer numbers were selected to achieve the most force pulses possible. Even so, the result was a fast stepping up of the force to approximate a linear profile. As an example, this profile is displayed for the $m = 0.27$ bearing with a unit load of 0.745 bar in Fig. 30. Using this load condition yielded the results shown in Fig. 31.

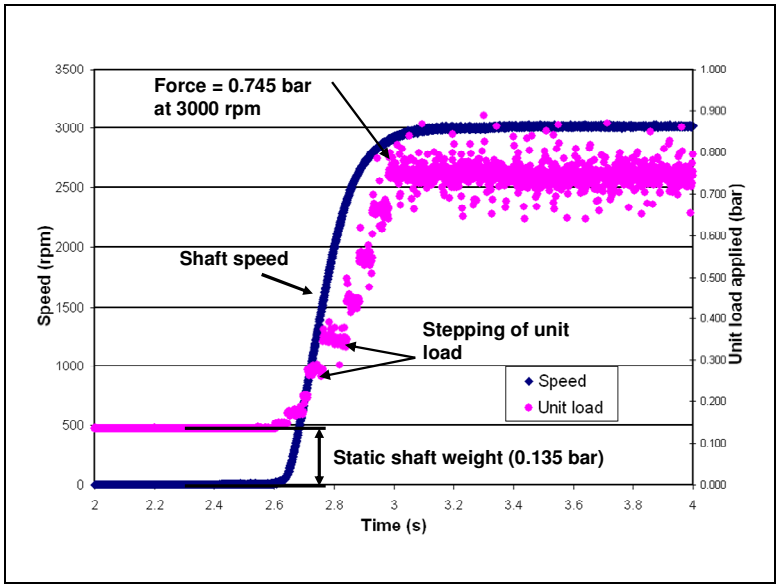

Fig. 30 Linear unit load force input to system (*m* = 0.27, 0.745 bar unit load, 0.689 bar supply pressure).

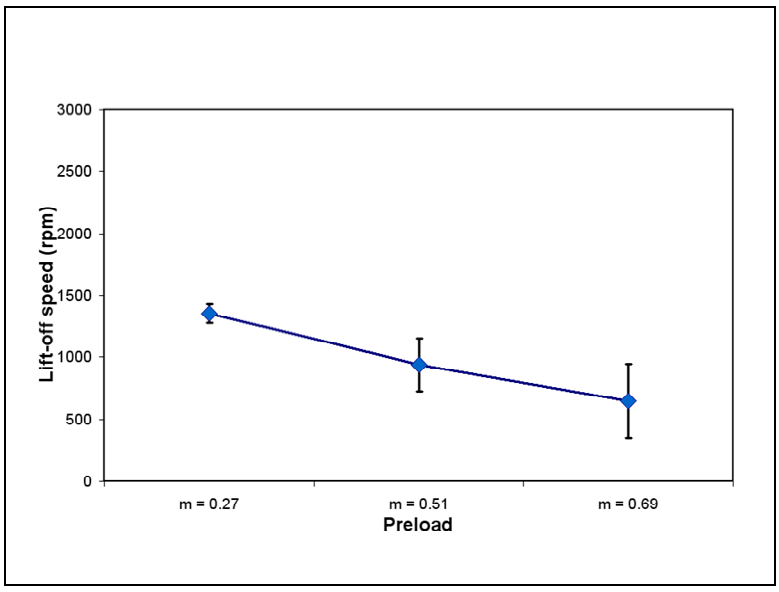

Fig. 31 Lift-off speed comparison for 0.745 bar unit load increasing linearly with time for 0.689 bar supply pressure (design speed = 3000 rpm).

The general trend is decreasing lift-off speed with increasing preload. Predictions were not made for the linearly increasing load cases because only static loads could be entered into XLHydroJet® for lift-off prediction. As previously stated,

predictions are based on the load capacity and the code does not give a lift-off speed result directly.

Lift-off Comparison to HHB

For comparison to the FPBs, a HHB is also tested in the LBP configuration. This particular HHB has pockets rather than pads. The procedure for testing is the same as that used for the FPBs with the exception of the supply pressure. Instead of using a static supply pressure as was used for the FPBs, a linearly increasing pressure profile was used. The supply pressure started at zero and increased linearly with speed up to a maximum pressure. Three different maximum pressures were chosen: 0.689 bar, 2.72 bar, and 5.52 bar. The pressure profiles for each design speed (linearly increasing to 0.689 bar) are shown in Fig. 32 - Fig. 35. For comparison with the FPB supply pressures, refer to Table 5.

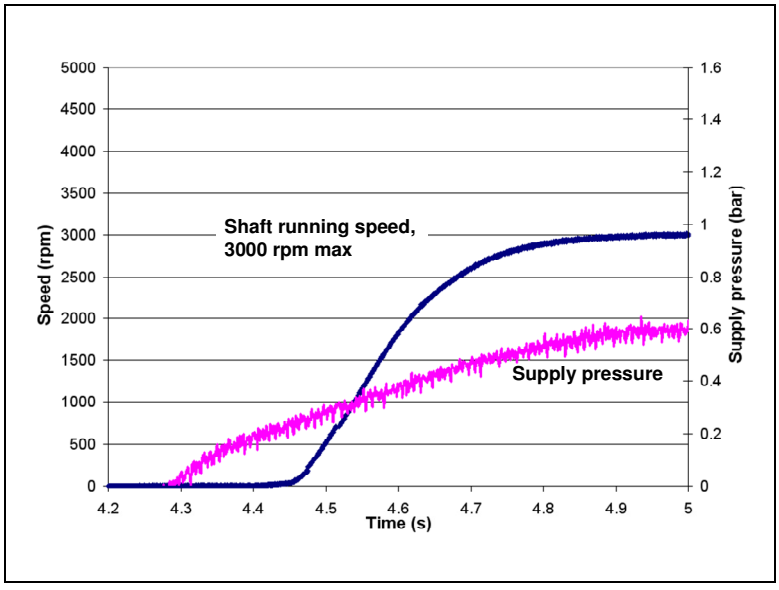

Fig. 32 HHB supply pressure profile ramp to 0.689 bar (3000 rpm design speed).

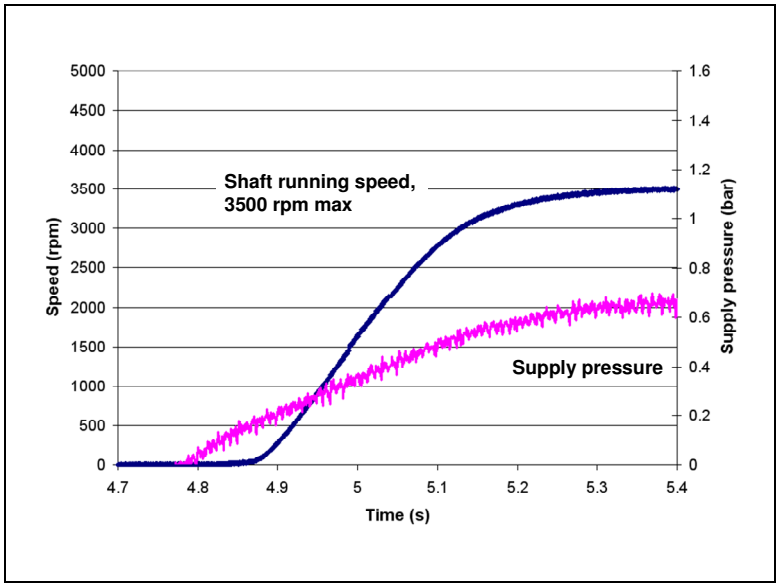

Fig. 33 HHB supply pressure profile ramp to 0.689 bar (3500 rpm design speed).

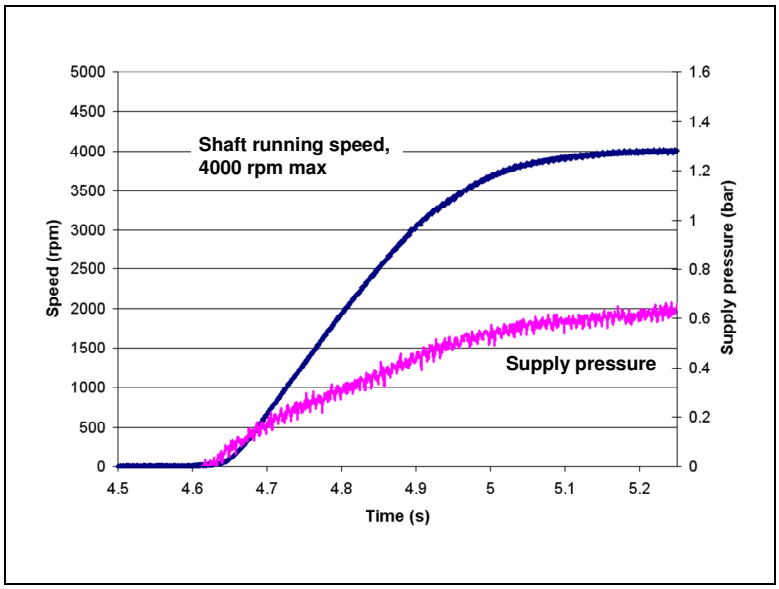

Fig. 34 HHB supply pressure profile ramp to 0.689 bar (4000 rpm design speed).

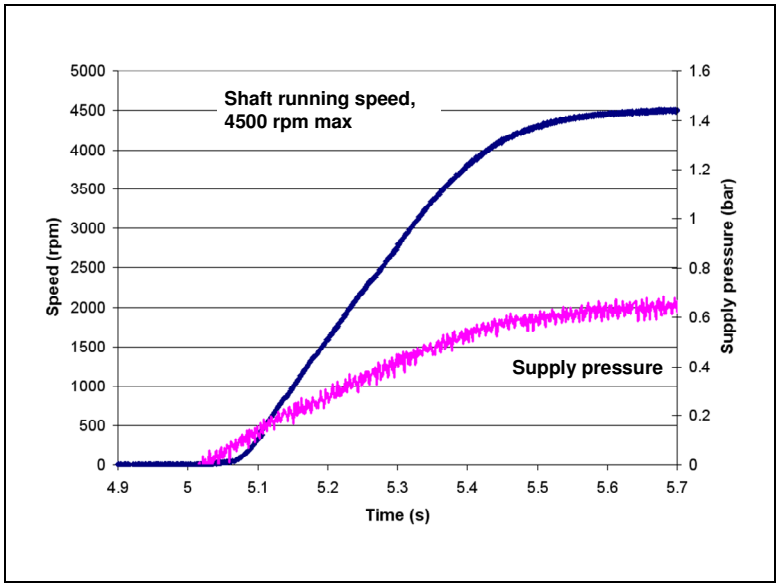

Fig. 35 HHB supply pressure profile ramp to 0.689 bar (4500 rpm design speed).

With respect to the start of the running speed profile, the pressure profiles did not start at the same point consistently. Variation in the start time of the pressure profile would be approximately 0.15 second on either side of the start time of speed profile. This variation even occurred for the exact same test cases. Since the HHB is pressure dependent, this greatly influences the results.

Lift-off results are tabulated for the range of running speeds previously described. The load profiles were adjusted to reach the maximum load at different design speeds. *The design speed is the final running speed of the shaft for a particular test case.* Unfortunately, the motor took different periods of time to reach each design speed. In fact, it took slightly longer to reach the higher design speeds. That is, there are different acceleration rates for the same applied unit load.

An increasing acceleration with increasing design speed is shown in Fig. 36. Physically, this means that the bearings with greater acceleration experienced the same loads at higher running speeds than those with lower accelerations.

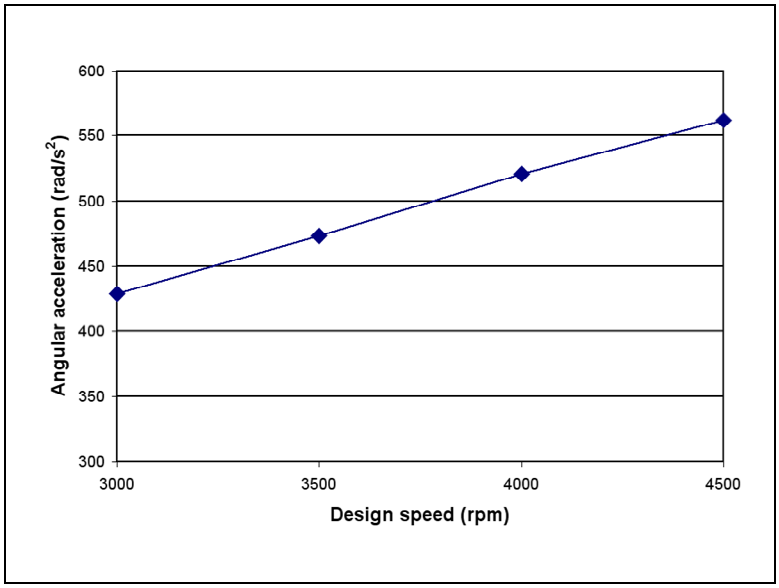

Fig. 36 Shaft angular acceleration for selected design running speed.

The example shown in Fig. 37 illustrates variation of lift-off speed with design speed. Both FPBs and HHBs are shown on the same graph for comparison.

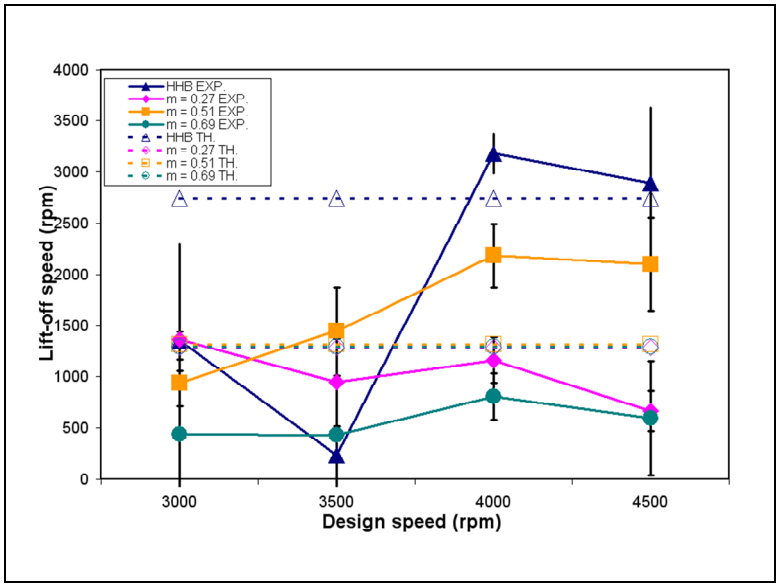

Fig. 37 Lift-off speed vs. design speed comparison for 0.745 bar linearly increasing unit load (0.689 bar linear supply pressure for HHB, 0.689 bar static pressure supply for FPBs, LBP configuration).

The results (labeled EXP. in the legend) show no clear trends, and thus no conclusion can be made about the individual bearings. However, there are large jumps in the HHB. This graph shows that the HHB is highly pressure dependent. Based on the previous pressure profile plots, the start time of the pressure ramp severely affects the lift-off speed in the HHB. As noted in Fig. 32 - Fig. 35, the supply pressure was difficult to control.

The theoretical lift-off speeds shown in Fig. 37 are based on the load capacity predictions in XLHydroJet®. The load was increased linearly with time for these test cases. However, for the predictions, a static maximum load of 0.745 bar was applied, and the lift-off speed calculated for this load condition.

Since the HHB is pressure dependent, a single pressure profile case and speed ramp case is chosen for comparison with the FPBs. The shaft weight-only case at 3000 rpm will be used. Since the HHB could only be placed in the bearing housing in the LOP position, this orientation is compared to the FPB in the LBP position. Unfortunately, the LBP position was the only available orientation position for the FPB. LBP tests for the HHB could only be performed by applying an external side load with the magnetic bearing. The test case for 0.689 bar supply pressure and 0.135 bar unit load is shown in Fig. 38.

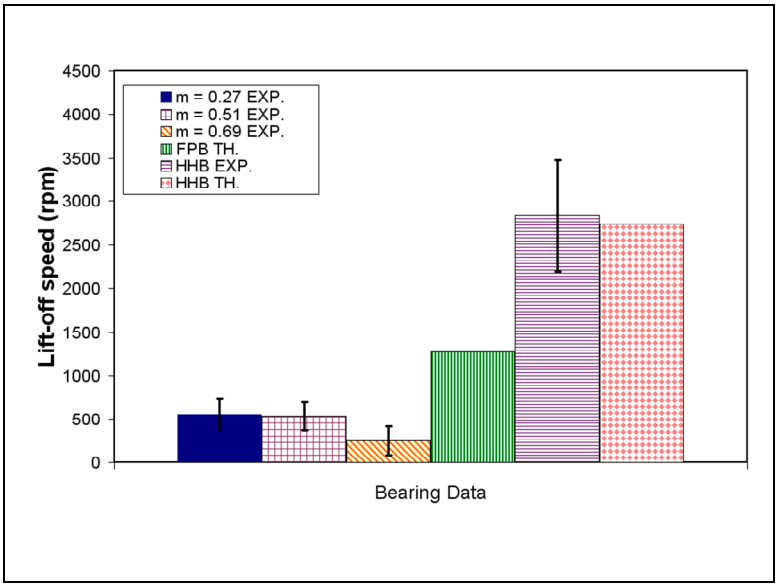

Fig. 38 Comparison of FPB vs. HHB for shaft weight-only case (0.135 bar unit load). LOP at 4500 rpm design speed for HHB and LBP at 3000 rpm design speed for FPBs. Supply pressure is 0.689 bar linearly increasing for HHB and static 0.689 bar for the FPBs.

When comparing the two types of bearings without load from the magnetic bearing, it is clear that the FPBs have a much lower lift-off speed. The superior hydrodynamic ability of the FPBs is evident as it lifts the shaft much earlier than the HHB does. The predictions for the HHB are very close but the predictions for the FPBs are more than double the measured results.

Increasing the supply pressure in the HHB yields lift-off results similar to the FPBs. As shown in Fig. 39, the lift-off speed decreases substantially for an increase in supply pressure. The predicted lift-off speed is much lower than the speed shown in the results.

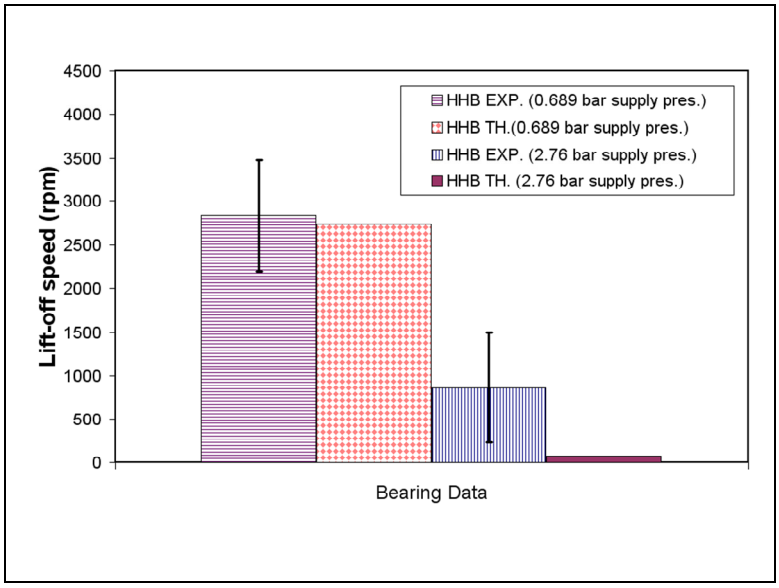

Fig. 39 HHB lift-off speed results for increasing supply pressure. (Design speed = 3000 rpm, 0.135 bar static unit load).

Maximum Unit Load Test Results

When the linearly increasing load was applied to the shaft, in most cases the FPB did not support the maximum load. Instead, the shaft was forced back into contact with the bearing as illustrated by Fig. 40.

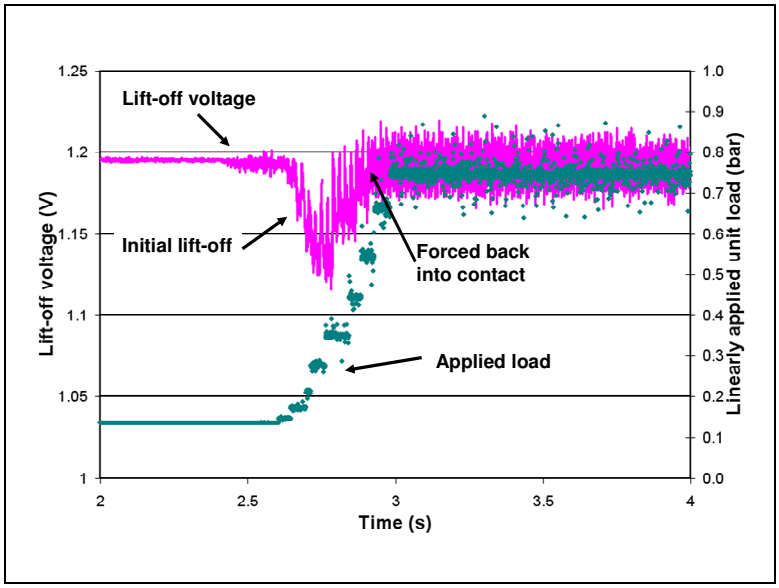

Fig. 40 Lift-off, then contact in FPB (*m* = 0.27, 0.745 bar unit load, 0.689 bar supply).

The bearing lifted off under lower loads and then came back into contact as the load increased. The *maximum load supported* by the bearing was recorded as the last load before the shaft re-contacts the bearing surface. If the bearing did not re-contact, then the maximum load recorded was the load at the design speed of the bearing. Since the load was increased linearly until it reached its maximum at the design speed, the maximum load in this case would also be the maximum load applied.

The average load supported by each bearing is shown in Fig. 41 for the 0.745 bar unit load case.

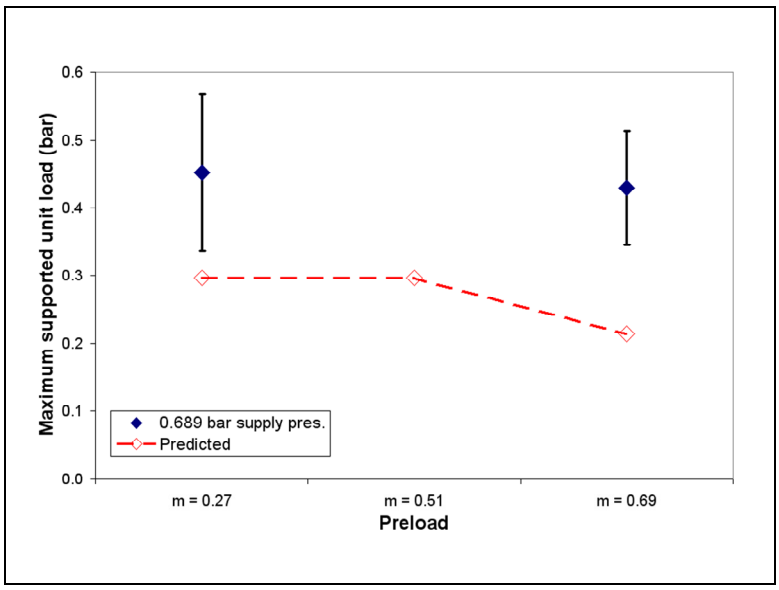

Fig. 41 Maximum unit load supported for various preloads in FPBs (0.745 bar linearly increasing unit load at 0.689 bar supply pressure, design speed = 3000 rpm).

Generally, the $m = 0.27$ bearing shows the highest load capacity, while the $m = 0.69$ bearing showed a slightly lower load capacity. The $m = 0.51$ bearing did not support any load at this supply pressure. It did support load at higher supply pressures, but it still had the worst load capacity of all three FPBs. A figure showing results for all the supply pressures is provided in the Appendix.

Comparing the FBP to the HHB at the 0.689 bar supply pressure proved difficult. The HHB did not lift-off until higher running speeds, so the chart in Fig. 42 compares the bearings at a design speed of 4500 rpm.

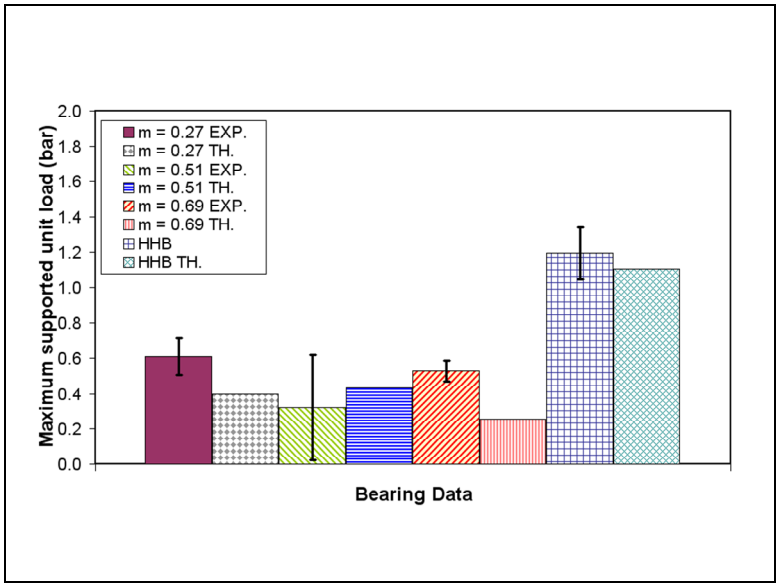

Fig. 42 Comparison of FPB and HHB maximum supported unit load for design speed = 4500 rpm, 0.689 bar supply pressure (static for FPB, linearly increasing for HHB), LBP configuration, 1.380 bar linearly applied unit load.

The results indicate that the HHB supports at least twice the load that the FPBs do. The maximum applied load in this case is 1.380 bar, and this is supported by the HHB. The load capacity of the HHB is superior to that of the FPBs.

Eccentricity Ratios

The only load profile where final eccentricities were obtained for the FPBs was for the 0.135 bar static unit loading case. The other cases loaded the shaft so that it remained in contact with the bearing. Since the shaft can rub outside of the C_b with the movement of the pads, this resulted in calculated eccentricities greater than one. The 0.135 bar static unit load case gave eccentricity ratios at 3000 rpm as shown in Fig. 43**.**

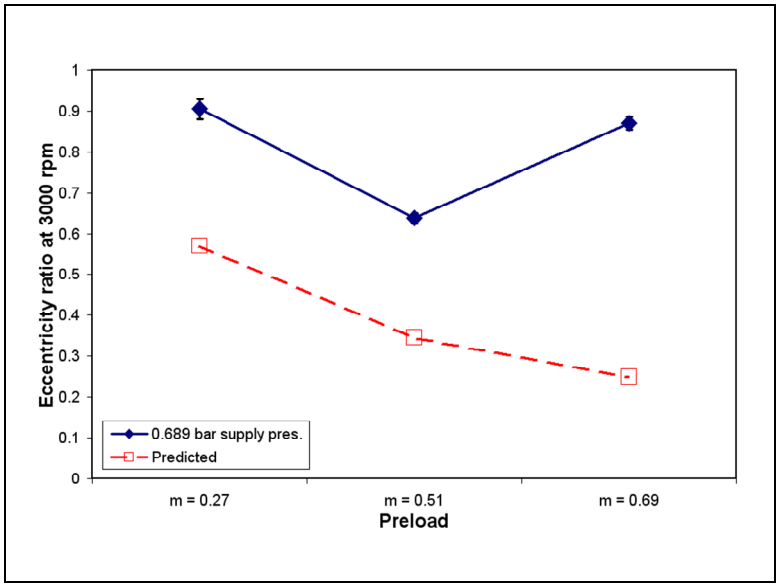

Fig. 43 Final eccentricity ratios for 0.135 bar unit load at 3000 rpm, 0.689 bar pressure supply in a FPB.

The lower the eccentricity ratio, the closer the shaft is to the bearing center. High eccentricities operate near the bearing surface and are more prone to rub. The predictions show a decreasing eccentricity ratio with increasing preload. This matches the trend found in the FPB results for the $m = 0.27$ and $m = 0.51$ case but is in conflict with the $m = 0.69$ results.

The results for the HHB compared to the FPBs at a linearly increasing 0.689 bar supply pressure are shown in Fig. 44.

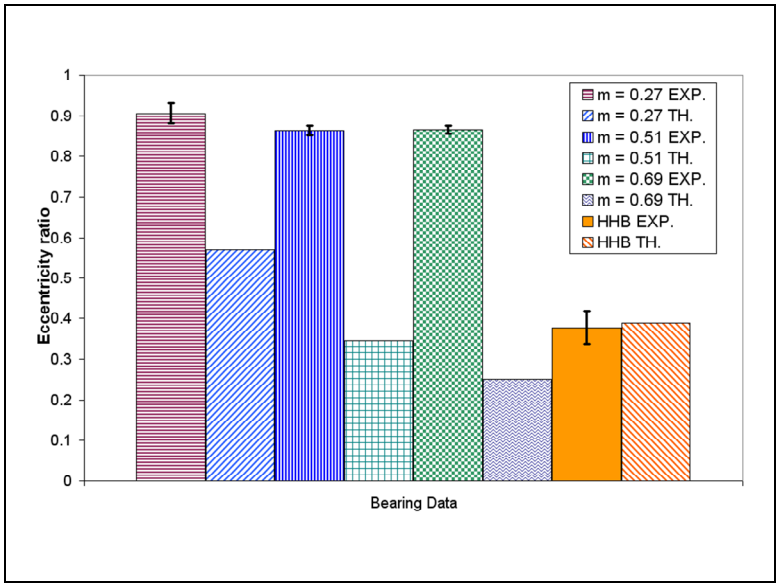

Fig. 44 Comparison of HHB and FPB at 3000 rpm, shaft weight-only case (0.135 bar unit load). Supply pressure is static at 0.689 bar for FPBs and linearly increasing to 0.689 bar for the HHB. Orientation is LBP for FPBs and LOP for HHB.

The HHB has much lower eccentricities than the FPB for the shaft weight-only case. Due to the bolthole arrangement in the bearing housing, the orientations of LBP for FPBs and LOP for HHB were the only ones possible when considering the shaft weight-only case. Future experiments should orient the shaft weight directly between the pockets for the HHB to confirm that its eccentricity ratio is still lower than the FPBs'.

Attitude Angle

The attitude angle indicates the position of the shaft with respect to the load. For the FPBs, the load was applied downward in the vertical direction. Due to the orientation of the HHB, however, the load was applied as a horizontal side load to achieve a load-between-pocket configuration instead of a load-on-pocket. During experiments, the attitude angle did not vary with supply pressure significantly for the FPBs. Thus, the 3000 rpm, 0.689 bar supply pressure is chosen for results shown in Fig.

45. These results show the LOP configuration of the HHB since that was the only configuration available for the shaft weight-only case.

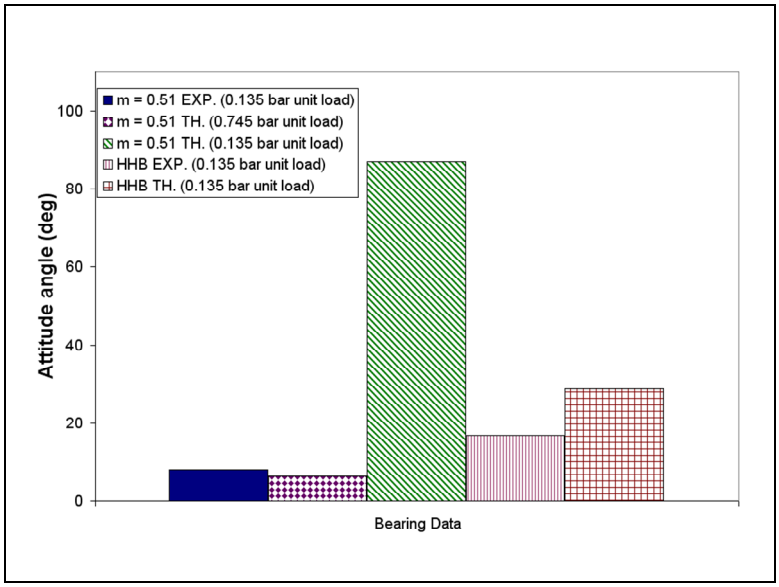

Fig. 45 Attitude angle comparison for HHB (LOP) and *m* = 0.51 (LBP) for 3000 rpm and 0.689 bar supply pressure.

Attitude angles are slightly lower for the FPB than the HHB. In comparison to the predictions for the 0.135 bar unit load case, results are much lower than the predicted attitude angle. The simulations showed the shaft moving in the horizontal direction for light loads, which is indicative of no cavitation. Increasing the unit load to 0.745 bar achieves predicted attitude angles closer to the experimental results.

The predictions for the HHB do vary with supply pressure, which is consistent with the experimental results for higher load cases. A very good match between predicted (TH.) and experimental (EXP.) results is confirmed in Fig. 46. The shaft was placed under a side load in order to maintain a LBP configuration. Hence, lower loads were not available for the LBP configuration.

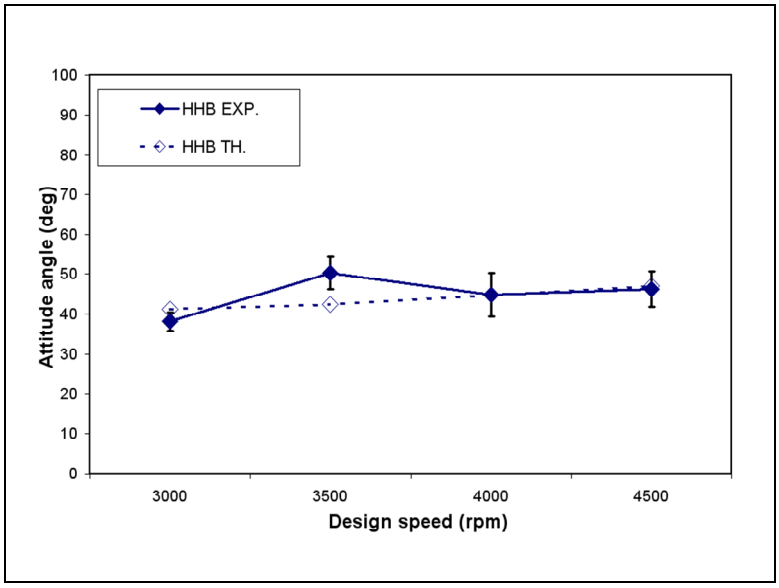

Fig. 46 Comparison of HHB attitude angles (LBP, 0.745 bar unit load, 0.689 bar supply).

Comparison Between Water and Kerosene for FPBs

The system conditions are meant to simulate a turbopump operating with kerosene as a lubricant. Since a closed loop kerosene system was not available for the testing, water was used in its place. From the kinematic viscosities in Table 10, kerosene is more viscous than water by a factor of 2.1. However, water is 2.2 times more viscous than liquid methane.

Table 10 Comparison of water and kerosene

Property	Water	Kerosene	Liquid Methane
Temperature (ºC)	40 (104ºF)	40 (104ºF)	-165 (-265ºF)
Pressure (bar)	1 (14.5 psia)	1 (14.5 psia)	1 (14.5 psia)
Density (kg/m^3)	992.22 (61.942 lbm/ft^3)	815.5 (50.912 lbm/ft^3)	427.46 (26.686 lbm/ft^3)
Dynamic viscosity (µPa-s)	652.98 (0.65298 cP)	1130 (1.13 cP)	126.8 (0.1268 cP)
Kinematic viscosity (cSt)	0.658	1.386	0.297

Kerosene is more viscous and will have a better performance than water or liquid methane. Predictions confirm this and details can be found in the Appendix.

Evaluating the rotational Reynolds numbers gives further insight into the differences in lubricating fluid. The equation for the Reynolds number is [1]:

$$\mathrm{Re} = \frac{\Omega R C_b}{\nu}. \tag{10}$$

According to Table 11, the flow is laminar for all the bearings. However, lower viscosity liquid methane has the highest Reynolds numbers.

Table 11 Reynolds numbers for water, kerosene, liquid methane

Bearing	RPM	Water Re	Lam/Turb	Kerosene Re	Lam/Turb	Methane Re	Lam/Turb
0.27	3000	18	Lam	8	Lam	39	Lam
0.27	3500	21	Lam	10	Lam	46	Lam
0.27	4000	24	Lam	11	Lam	52	Lam
0.27	4500	26	Lam	13	Lam	59	Lam
0.51	3000	22	Lam	10	Lam	48	Lam
0.51	3500	25	Lam	12	Lam	56	Lam
0.51	4000	29	Lam	14	Lam	64	Lam
0.51	4500	32	Lam	15	Lam	72	Lam
0.69	3000	37	Lam	18	Lam	83	Lam
0.69	3500	44	Lam	21	Lam	97	Lam
0.69	4000	50	Lam	24	Lam	110	Lam
0.69	4500	56	Lam	27	Lam	124	Lam
HHB	3000	11	Lam	5	Lam	24	Lam
HHB	3500	13	Lam	6	Lam	29	Lam
HHB	4000	15	Lam	7	Lam	33	Lam
HHB	4500	17	Lam	8	Lam	37	Lam

6. SUMMARY

Several different methods for detection of lift-off speeds were performed in these experiments. The most basic method is to evaluate the shaft centerline plots and view the upward motion of the shaft. A measured bearing clearance is required to determine the lift-off speed. The main problem with this method is that there can be uncertainties not only in the motion of the shaft but also in the measured bearing clearance.

The next method, which proved more reliable, was to look at the vibration frequencies of the bearing housing as the shaft accelerates. Accelerometers on the bearing housing showed supersynchronous frequencies that dropped off as the shaft lifted upwards. When comparing these frequencies to running speed, it was difficult to ascertain the exact speed of lift-off. Several high-level frequencies developed but did not all drop off at the same time consistently.

The final method and the one selected for determination of lift-off speed, was to measure the voltage across a resistor in a shaft circuit. When the shaft lifted off, the voltage drop across the resistor was significant enough to give a consistent lift-off speed measurement. Problems with this method include noise in the shaft circuit and assumptions as to when to consider the shaft fully lifted off. Since the shaft may initially lift up slightly then fall back in contact, the exact lift-off point was defined to be the point where the voltage dropped 0.05 volts from the mean value for at least 8 ms. This point was chosen as a conservative estimate to yield consistent results regardless of the noise in the signal. Future experiments may wish to refine these assumptions.

7. CONCLUSIONS

In comparison to load-capacity-based predictions for FPBs, the experimental results showed lower lift-off speeds, higher load capacities, higher eccentricity ratios, and lower attitude angles. Load capacity does appear to affect lift-off speed but no clear trend was found. Hence, lift-off speed is poorly predicted from load capacity.

Some factors that future experiments need to consider are pressure dependency and design speed. The *design speed* is the maximum running speed achieved for a particular test run. The FPBs unexpectedly proved to be highly pressure dependent due to an end-seal phenomenon. Since the HHB is also pressure dependent, changing design speeds with linearly increasing force and pressure profiles was difficult to perform consistently. In these experiments, increasing design speed also increased the acceleration of the shaft.

Another difficultly arose in the form of orientation. Due to the design of the bearing housing, the HHB could only be placed in the LOP position and the FPB in the LBP position. External loads were applied to the shaft for the HHB test cases to compare the LBP positions for both bearings.

The HHB showed greater load capacity and lower eccentricities than the FPBs, but the FPBs had lower lift-off speeds and attitude angles. This comparison is for a 0.689 bar supply pressure and 3000 rpm design speed. At this supply pressure and considering the shaft weight-only case, the FPB in the LBP orientation had much lower lift-off speeds than the HHB in the LOP orientation. Increasing the supply pressure to the HHB decreased its lift-off speed to much lower levels. Hence, for lower supply pressures, the FPB outperformed the HHB in terms of lift-off speed. If the load capacity needed in the bearing application remains relatively small, a FPB could replace an HHB.

REFERENCES

[1] San Andrés, L., 2006, "Modern Hydrodynamic Lubrication Theory," Texas A&M University MEEN 626 Class Notes. http://phn.tamu.edu/me626. Access date: May 2007.

[2] Childs, D. and Al-Ghasem, A., 2006, "Rotordynamic Coefficients Measurements Versus Predictions for a High-Speed Flexure-Pivot Tilting-Pad Bearing (Load-Between-Pad Configuration)," *J. Eng. Gas Turb. Power*, **128**, pp. 896-906.

[3] Chen, W. J., 1995, "Bearing Dynamic Coefficient of Flexible Pad Bearings," *Tribol. T.*, **38**(2)**,** pp. 253-260.

[4] Childs, D., 1993, "Turbomachinery Rotordynamics: Phenomena, Modeling, and Analysis," John Wiley, New York.

[5] Kepple, W. E., Read, D. W., Zeidan, F. Y., Paraskevakos, C., and Dawson, M. P., 1998, "Experience in the Use of Flexure Pivot Tilt Pad Bearings in Boiler Feed Water Pumps," *Proceedings of the 15th International Pump Users Symposium*, Turbomachinery Laboratory, College Station, TX, pp. 77-84.

[6] Rodriguez, L., 2004, "Experimental Frequency-Dependent Rotordynamic Coefficients for a Load-On-Pad, High-Speed, Flexible-Pivot Tilting-Pad Bearing," M.S. thesis, Texas A&M University, College Station, Texas.

[7] Zeidan, F., 1992, "Developments in Fluid Film Bearing Technology," *Turbomach. Int.*, **9**, pp. 24-31.

[8] San Andrés, L., 1996, "Turbulent Flow, Flexure-Pivot Hybrid Bearings for Cryogenic Applications," *ASME J. Tribol.*, **118**(1), pp. 190-200.

[9] "XLTRC^2: Rotordynamics Software Suite," The Turbomachinery Laboratory, Texas A&M University. http://turbolab.tamu.edu/research/trc/XLTRC%202002.pdf. Access date: August 2008.

[10] "XLHYDROJET: Computational Analyses of Hydrostatic/Hydrodynamic Bearings," Texas A&M University. http://phn.tamu.edu/TRIBGroup/Soft_hydrojet_1.htm. Access date: August 2008.

[11] Zeidan, F. and Paquette, D., 1994, "Application of High Speed and Higher Performance Fluid Film Bearings in Rotation Machinery," *Proceedings of the 23rd Turbomachinery Symposium*, Turbomachinery Laboratory, Texas A&M University, Dallas, TX, pp. 209-234.

[12] De Choudhury, P., Hill, M., and Paquette, D., 1992, "A Flexible Pad Bearing System for a High Speed Centrifugal Compressor," *Proceedings of the 21st Turbomachinery Symposium*, Turbomachinery Laboratory, Texas A&M University, Dallas, TX, pp. 57-64.

[13] Armentrout, R., and Paquette, D., 1993, "Rotordynamic Characteristics of Flexure-Pivot Tilting-Pad Journal Bearings," *Tribol. T.*, **36**(3), pp. 443-451.

[14] Elwell, R. C., and Findlay, J. A., 1969, "Design of Pivoted-Pad Journal Bearings," *ASME J. Lubric. Tech.*, **91**(1), pp. 87–103.

[15] Wygant, K., Flack, R., and Barrett, L., 2004, "Measured Performance of Tilting-Pad Journal Bearings over a Range of Preloads—Part 1: Static Operating Conditions," *Tribol. T.*, **47**, pp. 576-584.

[16] Scharrer, J.K., Tellier, J.G., and Hibbs, R.I., 1991, "A Study of the Transient Performance of Hydrostatic Journal Bearings: Part II-Experimental Results," STLE/ASME Tribology Conference, STLE Paper 91-TC-3B-2, St. Louis, MO, pp. 1-7.

[17] Zhu, X., 2004, "Experimental Response of a Rotor Supported on Rayleigh Step Bearings," M.S. thesis, Texas A&M University, College Station, TX.

[18] Lu, X. and Khonsari, M. 2005, "On the Lift-off Speed in Journal Bearings," *Tribol. Lett.*, **20,** pp. 299-305.

[19] Bouyer, J., Fillon, M., and Pierre-Danos, I., 2006, "Influence of Wear on the Behavior of a Two-lobe Hydrodynamic Journal Bearing Subjected to Numerous Start-ups and Stops," *Proceedings of IJTC2006 STLE/ASME International Joint Tribology Conference,* San Antonio, TX.

[20] ASME B46.1-2002 *Surface Texture (Surface Roughness, Waviness, and Lay),* American Society of Mechanical Engineers (ASME), New York.

[21] Dyck, B.J., 2007. "Experimental Study of Dry-friction Whirl and Whip for a Rotor Supported by an Annular Rub Surface," Master's report, Texas A&M University, College Station, TX.

APPENDIX

The pad web is assumed to be a beam to determine the rotational web stiffness of each pad on the FPB. With the beam defined according to Fig. 47, Eqs. 11 and 12 can be used to the rotational web stiffness.

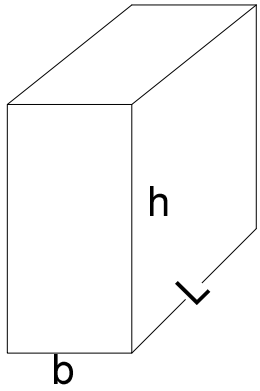

Fig. 47 Simple beam definition.

$$I = \frac{bL^3}{12} \tag{11}$$

$$K_\theta = \frac{4EI}{h} \tag{12}$$

Table 12 shows the measured bearing web geometry and calculated stiffness. Since K_θ is below 1000 N-m/rad, the bearing should behave as a TPB [5].

Table 12 Beam calculation results

Parameter	Value	Units
b	0.508 (0.02)	mm (in)
h	1.905 (0.075)	mm (in)
L	38.1 (1.5)	mm (in)
E	110.3 (16)	MPa (ksi)
K_θ	542 (4800)	N-m/rad (lb-in/rad)

Table 13 Test matrix

Case	Preload	Max speed (rpm)	Load Orientation	Supply Pres. (bar)	Supply Pres. (psi)	Max unit load (bar)	Max unit load (psi)
1	0.27	3000	LBP	0.689	10	0.135	1.96
2	0.27	3000	LBP	2.76	40	0.745	10.80
3	0.27	3000	LBP	5.52	80	1.380	20.01
4	0.27	3000	LBP	0.689	10	0.135	1.96
5	0.27	3000	LBP	2.76	40	0.745	10.80
6	0.27	3000	LBP	5.52	80	1.380	20.01
7	0.27	3000	LBP	0.689	10	0.135	1.96
8	0.27	3000	LBP	2.76	40	0.745	10.80
9	0.27	3000	LBP	5.52	80	1.380	20.01
10	0.51	3000	LBP	0.689	10	0.135	1.96
11	0.51	3000	LBP	2.76	40	0.745	10.80
12	0.51	3000	LBP	5.52	80	1.380	20.01
13	0.51	3000	LBP	0.689	10	0.135	1.96
14	0.51	3000	LBP	2.76	40	0.745	10.80
15	0.51	3000	LBP	5.52	80	1.380	20.01
16	0.51	3000	LBP	0.689	10	0.135	1.96
17	0.51	3000	LBP	2.76	40	0.745	10.80
18	0.51	3000	LBP	5.52	80	1.380	20.01
19	0.69	3000	LBP	0.689	10	0.135	1.96
20	0.69	3000	LBP	2.76	40	0.745	10.80
21	0.69	3000	LBP	5.52	80	1.380	20.01
22	0.69	3000	LBP	0.689	10	0.135	1.96
23	0.69	3000	LBP	2.76	40	0.745	10.80
24	0.69	3000	LBP	5.52	80	1.380	20.01
25	0.69	3000	LBP	0.689	10	0.135	1.96
26	0.69	3000	LBP	2.76	40	0.745	10.80
27	0.69	3000	LBP	5.52	80	1.380	20.01
28	HHB	3000	LBP	0.689	10	0.135	1.96
29	HHB	3000	LBP	2.76	40	0.745	10.80
30	HHB	3000	LBP	5.52	80	1.380	20.01
31	HHB	3000	LBP	0.689	10	0.135	1.96
32	HHB	3000	LBP	2.76	40	0.745	10.80
33	HHB	3000	LBP	5.52	80	1.380	20.01
34	HHB	3000	LBP	0.689	10	0.135	1.96
35	HHB	3000	LBP	2.76	40	0.745	10.80
36	HHB	3000	LBP	5.52	80	1.380	20.01

Supplemental Figures

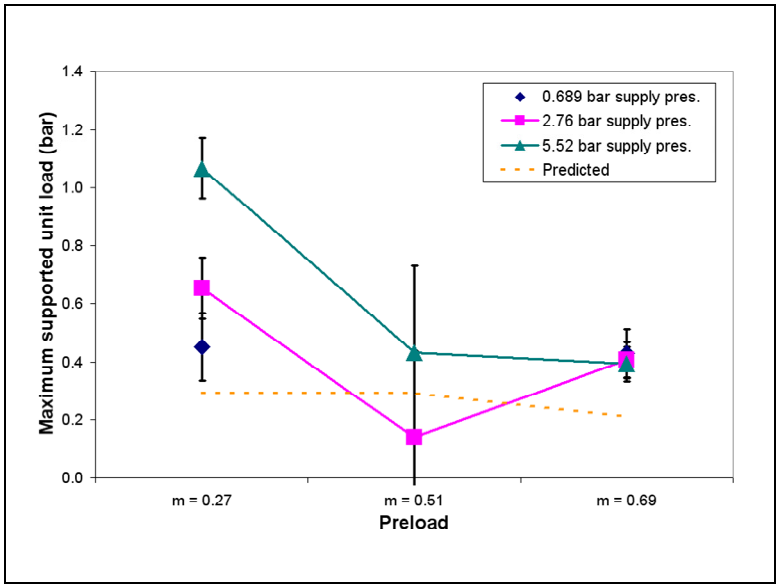

Fig. 48 Maximum unit load supported for 0.745 bar linearly increasing unit load.

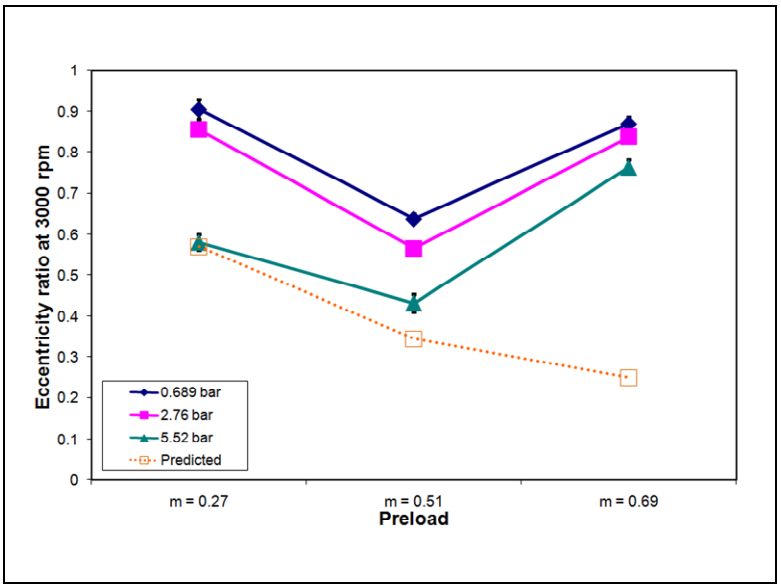

Fig. 49 Eccentricity ratio at 3000 rpm for various preloads compared to predictions.

Comparison of Water, Kerosene, and Liquid Methane

Since water is not the actual fluid that will be used in a turbopump application, it remains to be seen how changing the working fluid would change the system. A comparison of the predictions between water and kerosene follows. The experimental results for water indicate that the predictions for water will give a reasonable estimate as to its actual performance. Lift-off speeds for both water and kerosene are compared for various preloads in Fig. 50.

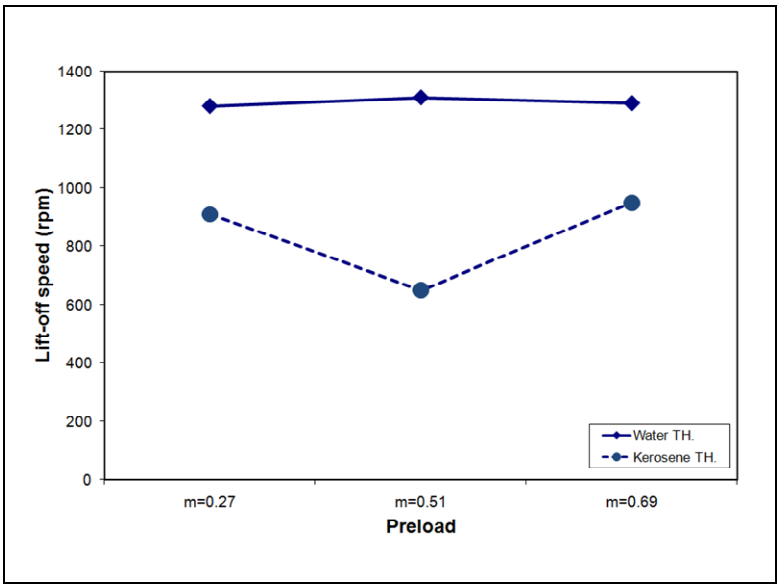

Fig. 50 Predicted lift-off comparison between water and kerosene (for constant C_b).

Kerosene has significantly lower predicted lift-off speeds than water. The increased viscosity of kerosene here seems to have a beneficial effect as lower lift-off speeds mean less bearing rub and resulting wear.

Next, the maximum load for FPBs for different lubricating fluids are compared. The results of this simulation can be found in Fig. 51.

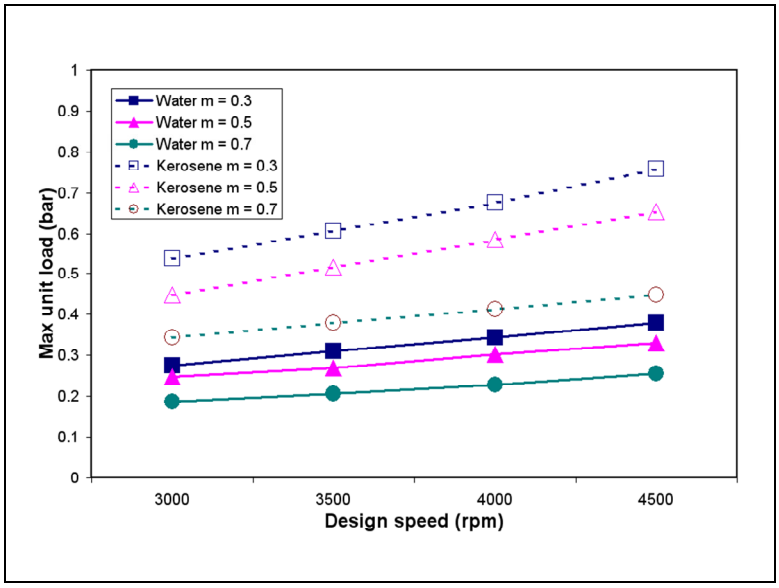

Fig. 51 Predicted max unit load comparison between water and kerosene (for a constant C_b).

Kerosene demonstrates higher load capacities for each bearing. Again, this effect would be beneficial to bearing operation. The effect on eccentricity ratios is shown in Fig. 52.

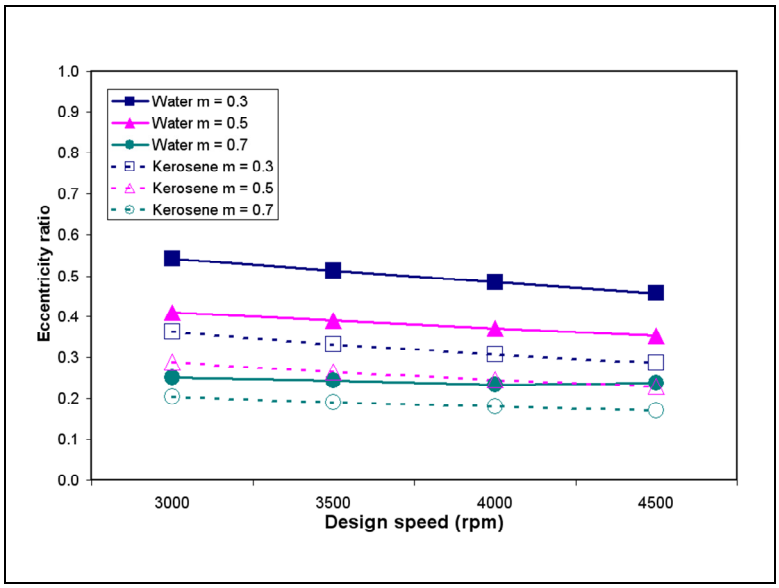

Fig. 52 Comparison of predicted eccentricity ratios between water and kerosene (for a constant C_b).

The lower eccentricity ratios for kerosene, in comparison with water, means that the shaft operates closer to the center of the bearing. Attitude angle comparisons in Fig. 53 show the kerosene having a slightly larger attitude angle than water. This confirms the predictions from the eccentricity ratios, indicating that the fluid film thickness in kerosene is larger than in water.

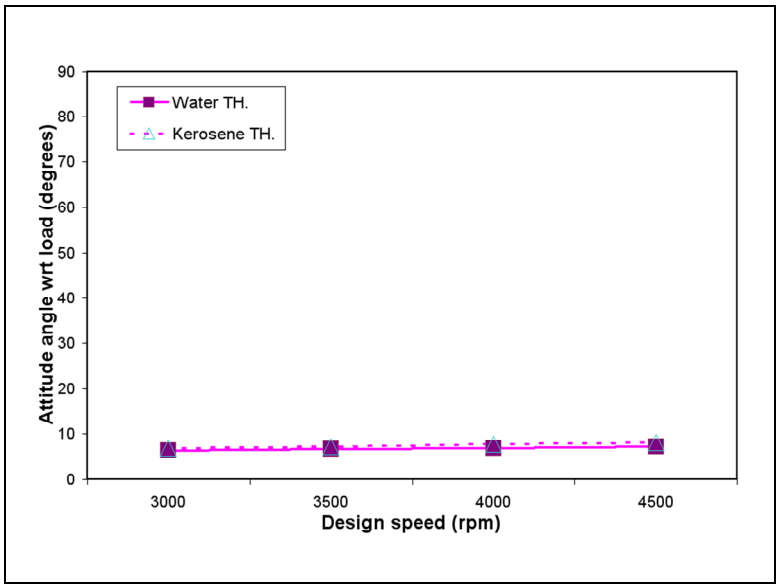

Fig. 53 Comparison of predicted attitude angle for water and kerosene (m = 0.51, 0.745 bar unit load, constant C_b).

From the previous simulated results, a kerosene-lubricated bearing would have an lower lift-off speed, higher load capacity, and higher shaft center operating position. Extrapolating these predictions to include liquid methane indicates that liquid methane would perform more poorly than both water and kerosene, since liquid methane has a kinematic viscosity 2.2 times smaller than water.

VITA

David Hunter Mertz
Department of Mechanical Engineering
3123 TAMU
College Station TX 77843-3123
david.h.mertz@gmail.com

Education:

M.S. Mechanical Engineering
December 2008
Texas A&M University

B.S. Engineering Science '06
Trinity University - San Antonio, TX

Work Experience:

Mechanical Engineer, Siemens Energy, Inc., Houston, TX

- Design of systems for gas turbines and compressors
- Conducted structural design analysis using FEA modeling in ANSYS
- Simulated process flows with HYSYS for oil and gas applications

Research Assistant, Texas A&M Turbomachinery Laboratory, College Station, TX

- Designed a flexure pivot pad bearing for lift-off testing
- Conducted rotordynamic tests on hybrid bearing designs for use in rocket engine turbopumps
- Installed and instrumented a water control valve for use in turbomachinery applications

Intern, American National Power, Midlothian, TX

- Designed a parking lot in AutoCAD while maintaining compliance with ADA code
- Implemented a safety relief valve inspection program in compliance with ASME code
- Studied aspects of the design of a combined cycle power plant